aerospace

MDPI

Article

Aerodynamic Effects of a Wing Surface Heat Exchanger

Anaïs Luisa Habermann [1,*], Ankit Khot [1], David Emanuel Lampl [2] and Christof Perren [1]

[1] Bauhaus Luftfahrt e.V., 82024 Taufkirchen, Germany; ankit.khot@tum.de (A.K.); christof.perren@tum.de (C.P.)
[2] Department of Aerospace and Geodesy, TUM School of Engineering and Design, Technical University of Munich, 85521 Ottobrunn, Germany; david.lampl@tum.de
* Correspondence: anais.habermann@bauhaus-luftfahrt.net

Abstract: One challenge for the design and analysis of hybrid electric aircraft configurations is an increased demand in the rejection of excess waste heat. A wing surface heat exchanger concept, which is explored as part of the IMOTHEP project, foresees transferring heat from the propulsive electrical components to the wing surface of the aircraft. Here, heat is mainly dissipated and transported by forced convection. The present study focuses on the analysis of the impact of heat rejection via the wing surface on the wing's heat transfer and aerodynamic efficiency characteristics. For this purpose, RANS CFD studies of 2D airfoils and a 3D wing propeller geometry of a regional turboprop configuration in representative flight conditions (take off, cruise, and taxi in) are carried out. For each condition, the influence of defining parameters, such as altitude, freestream velocity, angle of attack, surface temperature, and propeller thrust is explored. It is shown that, when increasing the wing surface temperature compared against the freestream temperature, the aerodynamic efficiency of the wing deteriorates for all flight conditions. In reference cruise conditions for example, the lift-to-drag ratio decreases by 4%, while the average heat transfer coefficient is reduced by almost 20% when increasing the surface temperature by 300 K. Furthermore, the propeller slipstream enhances the wing's heat transfer capacity significantly.

Keywords: wing surface heat exchanger; computational fluid dynamics; heated boundary layer; turbulent boundary layer; hybrid electric aircraft; IMOTHEP

check for updates

Citation: Habermann, A.L.; Khot, A.; Lampl, D.E.; Perren, C. Aerodynamic Effects of a Wing Surface Heat Exchanger. *Aerospace* **2023**, *10*, 407. https://doi.org/10.3390/aerospace10050407

Academic Editor: Anthony D. Gardner

Received: 16 March 2023
Revised: 14 April 2023
Accepted: 18 April 2023
Published: 27 April 2023

Copyright: © 2023 by the authors. Licensee MDPI, Basel, Switzerland. This article is an open access article distributed under the terms and conditions of the Creative Commons Attribution (CC BY) license (https://creativecommons.org/licenses/by/4.0/).

1. Introduction

The electrification of aircraft as an enabler for zero emission air transportation has been increasingly studied in recent years (see for example [1–6]). The introduction of electrical components as part of (hybrid) electric power trains increases the overall propulsion system efficiency. However, it is more difficult to remove the electrical waste heat from the aircraft compared to conventional propulsion systems, where the waste heat is removed through the exhaust air [7]. To keep the components within their safe operating temperature limits, their excess heat needs to be rejected. Designing an efficient thermal management system (TMS) poses one of the major challenges for (hybrid)electric aircraft [8]. Conventional TMSs use heat exchangers cooled by ram air. In contrast to that, unconventional TMSs foresee dissipating the heat, for example, over the wetted surfaces of the aircraft. Consequently, ram drag can be reduced [9]. For hybrid electric aircraft configurations, fuel might be used as the coolant for the TMS, thereby transferring heat from the electrical components inside the aircraft to the fuel tanks in the aircraft's wings [10]. The heated fuel then transfers the heat to the ambient air via the wing surface. This heat transfer process is caused by the temperature difference between fuel and ambient air as well as forced convection. In consequence, heat is introduced to the wing's boundary layer (BL), and the aerodynamic characteristics of the flow are altered.

The effect of uniform and non-uniform heating and cooling on the laminar and turbulent boundary layers of flat plates was extensively studied experimentally (e.g., [11,12]) and numerically (e.g., [13–15]) and is, thus, well understood. However, most studies focused on BLs with a zero pressure gradient and the usage of wall temperature alteration for BL

transition control as a means to reduce friction drag. For most aircraft components, the BL experiences a pressure gradient along the component surface. A number of numerical and experimental studies were conducted on fuselage-like bodies to investigate the drag control of fully turbulent BLs (e.g., [16,17]). The effect of surface temperature alteration on the BL of 2D and 3D airfoils was studied more thoroughly. Here, the purpose of most numerical and experimental studies was to assess the aerodynamic effect of thermal de-icing (e.g., [18,19]), the behavior of re-entry vehicles in subsonic conditions (e.g., [20,21]), and drag reduction through transition delay (e.g., [22]). Recently, Kallath et al. [23] employed a RANS CFD solver to systematically analyze how wing surface heating effects the BL of a symmetric 2D NACA 0012 airfoil. Local heat patches were employed to introduce heat to the fully turbulent BL at subsonic flow conditions ($Ma \leq 0.3$, $Re \leq 11.9 \times 10^6$). They confirmed that local heating alters the aerodynamics of the airfoil. However, the impact of surface heating on aerodynamics is insignificant at high Reynolds numbers, as the thickness of the thermal and velocity boundary layers is reduced. Depending on the location of the heat patches (lower or upper surface, leading or trailing edge), drag and lift can either be reduced or increased [23]. Literature on the combination of an enhanced forced convection with BL heating is scarce. Elsaadawy and Britcher [24] conducted wind tunnel experiments on a heat exchanger, which was embedded into the wing of an aircraft and subject to a propeller slipstream. The heat exchanger's air inlet was located at the leading edge of the wing; the ram air was released at the pressure side of the wing. During the study, the propeller was unpowered and free-wheeling at wind tunnel operating velocities [24].

It is apparent that existing studies in the field of aeronautics have focused on employing surface temperature alteration for thermal de-icing and flow control, especially transition delay. Few publications have analyzed the integrated effect of a wing surface heat exchanger (WSHX) application for flight conditions that are critical to the TMS of a regional turboprop configuration.

In this study, the effect of such a WSHX on the wing aerodynamics is investigated through numerical simulations. It is shown how the transfer of heat into the wing BL alters the relevant aerodynamic characteristics of the wing in different flight conditions that are representative for a regional aircraft (take off and cruise). Finally, the CFD simulation setup is used to investigate the so-called "REG-CON" hybrid electric aircraft configuration of the European-Union-funded Horizon 2020 IMOTHEP project (Investigation and Maturation of Technologies for Hybrid Electric Propulsion). For this hybrid electric aircraft concept, a TMS concept featuring a WSHX is explored as described above [25]. The present publication focuses on the analysis of the effect of this surface heat exchanger on wing aerodynamics and heat transfer efficiency.

The Reynolds-Averaged Navier Stokes Computational Fluid Dynamics (RANS CFD) solver SU2 [26] with a kω-SST turbulence model is validated against experimental data and another RANS CFD solver (OpenFOAM [27]) to systematically analyze heating the smooth surface of 2D airfoils and an unswept 3D wing in fully turbulent flow conditions. The following variations are assessed:

- Uniform heating of the whole airfoil surface and heating of local surface patches;
- The Reynolds number Re_c, Mach number Ma, and angle of attack α variation representing different flight conditions;
- Symmetric (NACA 0012) and asymmetric (modified NACA 4501X) airfoils with different thickness-to-chord ratios t/c;
- A 3D unswept wing with and without the effect of propeller slipstream in cruise, taxi and, take-off conditions.

2. Hybrid Electric Regional Aircraft with Wing Surface Heat Exchanger

A regional aircraft concept with hybrid electric propulsion (HEP) and a WSHX is the application case of the present study.

2.1. Aircraft Configuration and Thermal Management Concept

The IMOTHEP project investigates the emission reduction potential of hybrid electric power trains for commercial aircraft with an Entry-Into-Service slated for 2030+. Four aircraft configurations are identified and analyzed, which can potentially benefit from HEP [28]. The so-called "REG-CON" configuration is based on an existing ATR 42-600 aircraft with a twin turboprop propulsion architecture. The turboshaft engines feature a two-fold electric assistance from onboard batteries, which consists of the following: an electric drive of the compressor ("cycle-integrated parallel hybrid") [29] and an electric assistance to the power shaft ("mechanically-integrated parallel hybrid") [30] (Figure 1). A detailed presentation of the configuration is provided in [31]. Compared to conventional propulsion systems, which remove propulsive waste heat through the exhaust air, eliminating the electrical waste heat produced by the electrical components and battery poses a greater challenge. Additionally, it is more crucial to operate the electrical components and energy source within their safe temperature limits. For the present configuration, it is assumed that the operating temperature of the battery should not exceed 328 K throughout the whole mission, while the temperature of the power electronics is required to stay below 373 K. To efficiently make use of synergistic effects on aircraft level, an innovative TMS controls the thermal household of the REG-CON concept. Here, the aim is to limit the increase in mass, drag, and required additional power compared to conventional TMSs, which are based on compact Ram Air Heat EXchangers (R-HEXs).

On an aircraft level, various TMS architectures are investigated for the HEP application case, including R-HEXs and Surface Heat EXchangers (S-HEXs). The R-HEX can be scaled infinitely and is compact, which makes maintenance less challenging. The S-HEX, on the other hand, employs existing aircraft surfaces, which could reduce the degradation of the aircraft's aerodynamic efficiency. However, the applicability of the S-HEX is limited by low heat transfer rates under low-speed operating conditions with high power demand and corresponding high heat loads, such as take off or taxi in. To overcome this challenge, the aircraft concept utilizes the slipstream of the installed propellers to enhance heat transfer across the wetted external surface areas of the wing as sketched in Figure 1. In this region, the flow is considered to be fully turbulent. For the hybrid REG-CON aircraft, onboard fuel can be used as the coolant of the TMS, thereby transferring the heat from the electrical components inside the aircraft to the fuel tanks located in the aircraft's wings [9,10].

Both TMS solutions are considered and investigated in an integrated aircraft study, with the objective of finding a TMS that reliably removes all waste heat while having the least negative impact on the aircraft's performance in terms of block fuel. A first estimation found that, for the investigated configuration, the surface of the aircraft was sufficiently big to reject the battery and electrical component waste heat (>80 kW) over the S-HEXs. From a block fuel potential analysis, it was found, however, that it was most beneficial to combine a R-HEX with S-HEXs [31].

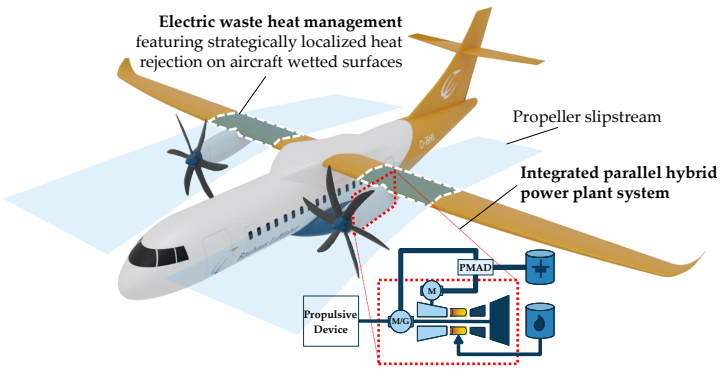

Figure 1. Visualization of the IMOTHEP REG-CON configuration. Source: [32].

2.2. Airfoil Selection

Detailed geometrical and aerodynamic characteristics of the ATR 42-600 wing profiles are unknown. However, publicly available data on the configuration indicate that the thickness-to-chord ratio t/c of the profile is 18% at the wing root and 13% at the wing tip [33]. A Finite Volume (FV) method solving the Euler equations coupled with a BL model called MSES (software for high lift multi-element airfoil configurations) [34] was used to study the five-digit NACA airfoil series. The results led to the selection of a slightly modified version of the NACA 45018 airfoil for the wing root and the NACA 45013 airfoil for the wing tip (see Figure 2).

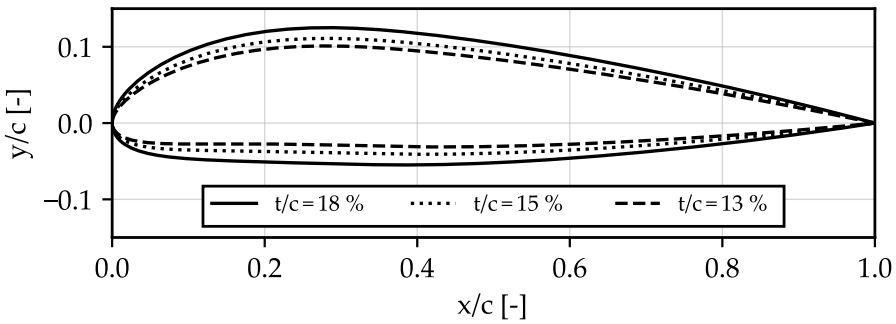

Figure 2. NACA 4501X airfoils with different t/c ratios. Axes true to scale.

The resulting airfoil characteristics were used in a wing aerodynamics study employing the nonlinear, steady-state lifting line tool PaWAT (Preliminary Design Tool for Propeller–Wing Aerodynamics) [35]. The results confirmed that the selected airfoils could meet the aerodynamic requirements of the ATR 42-600 aircraft for a range of cruise conditions ($C_L \approx 0.45$) as pictured in Figure 3. In the present study, the focus was on the unswept inboard section of the wing with the modified NACA 45018 airfoil.

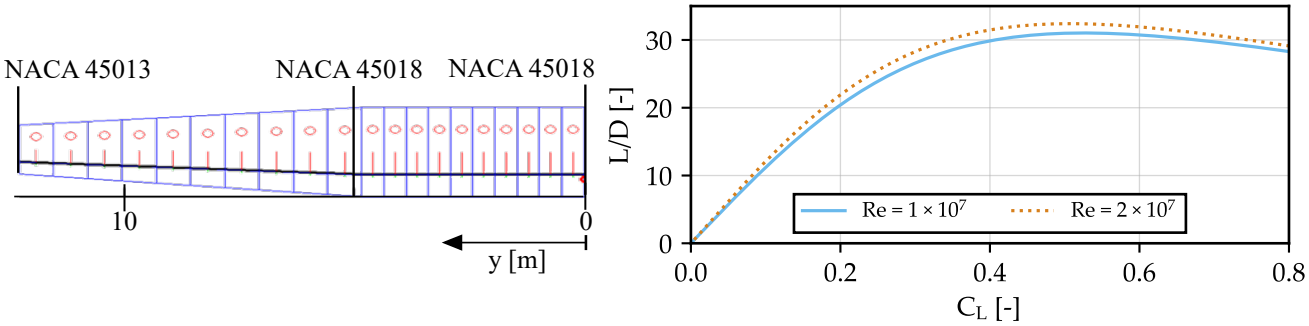

Figure 3. ATR 42-600 wing planform in PaWAT with airfoils at root, kink and tip section (**left**), and resulting lift-to-drag ratio L/D for a range of cruise Re_c (**right**).

3. Heat Transfer Effects on Aerodynamics

External heat transfer affects aerodynamics mainly due to the temperature viscosity and temperature density coupling effects [36]. Convective heat transfer is described, and its main aerodynamic effects are discussed below with respect to the heated wall case.

3.1. Convective Heat Transfer

Forced convection is the main mechanism of external heat transfer of a heated wing surface. In general, convective heat transfer is characterized by heat transfer due to conduction and energy transfer due to macroscopic movement of the fluid. In this context, the BL plays a fundamental role [37–39]. Figure 4 sketches the velocity and temperature profiles of a laminar, compressible, and attached BL with a zero pressure gradient in the flow direction. The discussed effects are analogous for turbulent BLs [39,40]. V_∞ and T_∞ denote the velocity and temperature of the freestream flow, respectively. The

heat transfer coefficient $h = \dot{q}_w/(T_w - T_{ad})$ results from the corresponding wall heat flux $\dot{q}_w$, the temperature difference of the wall surface temperature T_w, and the adiabatic wall temperature T_{ad} [38]. If dissipation is considered, the temperature of an adiabatic wall is higher than the freestream temperature, which is also called the adiabatic wall temperature T_{ad}. For turbulent boundary layers with a Prandtl number Pr close to unity, they can be computed using the recovery factor $r = Pr^{1/3}$ as $T_{ad} = T_\infty\left(1 + r\frac{\gamma-1}{2}Ma^2\right)$. Directly at the wall, energy is only transported by heat conduction and can, therefore, be described by Fourier's law, i.e., $\dot{q}_w = -k_w\,(\partial T/\partial y)\big|_w$. k_w is the thermal conductivity of the fluid at wall temperature, and $(\partial T/\partial y)\,|_w$ is the temperature gradient normal to the wall. As a consequence, the temperature distribution inside the BL is required to calculate k_w, which, in turn, is influenced by the BL velocity profile [38]. The Nusselt number $Nu = (hL)/k$ denotes the dimensionless heat transfer coefficient, which describes the ratio of convective to conductive heat transfer at a surface in a fluid. For external forced convection at subsonic speeds, the mean Nusselt number can be estimated by Re_c and Pr. Empirical correlations are often defined as power laws in the form of $Nu = C \cdot Re_c^{\,l} \cdot Pr^m \cdot (T_\infty/T_w)^n$ [38] with a constant C and the coefficients l, m, and n. The correction factor $(T_\infty/T_w)^n$ accounts for temperature-dependent fluid properties and is sometimes omitted [41].

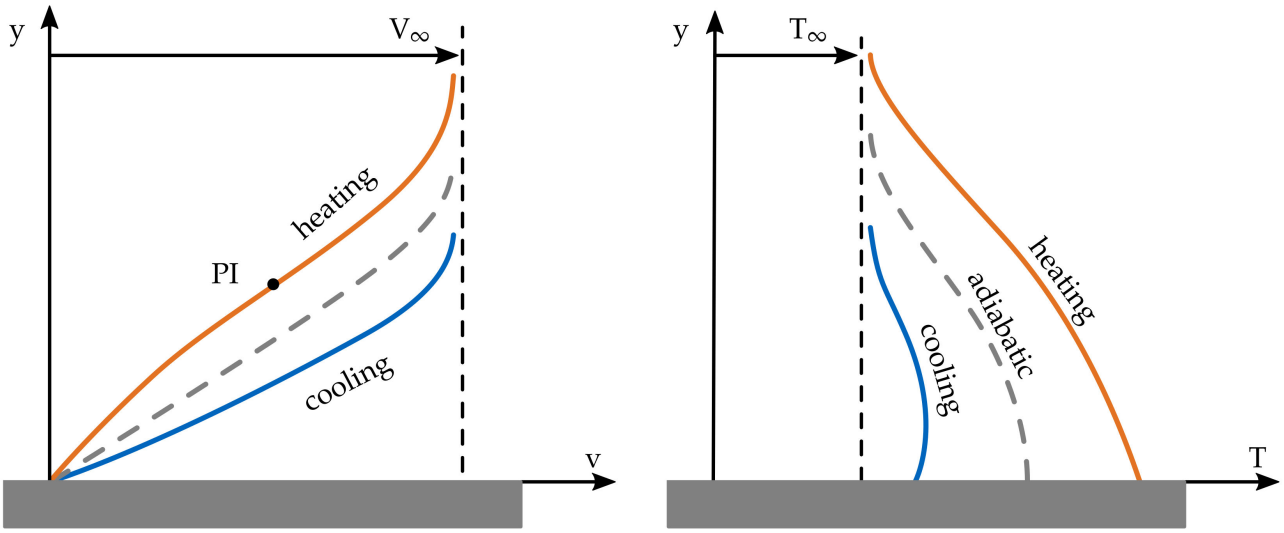

Figure 4. Velocity and temperature profiles in a compressible, attached laminar boundary layer with zero pressure gradient in flow direction (not to scale, based on [42]).

3.2. Consequences on Aerodynamics

The aerodynamic efficiency of an aircraft can be measured by the lift-to-drag ratio L/D [43]. Since the lift required during cruise is mainly dictated by aircraft weight, the only way to increase aerodynamic efficiency is to reduce drag [43]. For a two-dimensional airfoil below the critical Mach number, the total drag can be split into skin friction drag due to the shear stress distribution at the wall and pressure drag due to the pressure distribution [43]. On the one hand, heating reduces wall shear stress $\tau_w = \mu_w\,(\partial u/\partial y)\big|_w$, since the decrease in the velocity gradient normal to the wall dominates compared to the small increase in dynamic viscosity μ [40]. On the other hand, pressure drag increases due to the increase in BL thickness and the promotion of flow separation [20,40]. The increased BL thickness results from the reduction in density [40]. Figure 4 indicates that the curvature of the velocity $\partial^2 u/\partial y^2$ directly at the wall is positive, because the temperature and, thus, the viscosity gradient normal to the wall is negative. This can also be derived from the steady-state BL equations for the flat plate with a zero pressure gradient, which lead to $\left(\partial^2 u/\partial y^2\right)\big|_w \propto -(\partial\mu/\partial y)\big|_w$ [39].

Since the velocity curvature in the outer part of the BL is small but negative, a point of inflection (PI) inside the BL exists. The so-called PI criterion states that velocity profiles

with points of zero curvature are generally unstable and, thus, move the transition from laminar to turbulent flow further upstream, i.e., they reduce the amount of laminar flow. In the present study, the flow is characterized as fully turbulent and, consequently, the effects of heating on the transition from laminar to turbulent flow were not studied. Studies on the impact of heating on BL transition can be found in the literature (e.g., [37,39,44]). The existence of a PI is also directly related to the pressure gradient in the flow direction. Therefore, the effect of a heated wall on the BL stability is equivalent to that of an adverse pressure gradient. As a consequence, the resulting velocity profile is similar to a BL that is closer to flow separation [39]. Experiments on heated airfoils indicate that the increase in pressure drag prevails over the reduction in skin friction [20]. Moreover, since heating promotes flow separation, the maximum stall angle and maximum lift coefficient are reduced [20,21,45]. As a result, the maximum L/D diminishes at α in comparison to the adiabatic case [21]. However, simulations show that the decrease in skin friction can dominate at small α and high $\Delta T_w = (T_w - T_\infty)$, thus leading to a net reduction in the total drag [21]. Besides the influence on the aerodynamics, a moderate increase in α tends to result in a reduced h [19].

4. Simulation Setup

Numerical FV solvers were employed for the solution of the RANS equations. The simulation setups were validated against each other and against numerical and experimental validation data.

4.1. Numerical Solvers

Two numerical solvers were employed: SU2 and OpenFOAM. Turbulence was modelled by the two-equation k-ω-SST model. Transition was not modeled. Turbulence intensity I, which is defined as the ratio of the root-mean-square of the turbulent velocity fluctuations u' and the Reynolds-Averaged mean velocity U, was 0.1 for the 2D cases (to model the propeller slipstream effect) and 0.01 for the 3D cases. Thus, the effect of BL heating on transition alteration was not covered in this study. The BL was fully resolved for all cases ($y^+ < 1$). The air was assumed to be a calorically perfect gas. The properties were based on the International Standard Atmosphere (ISA) conditions [46]. The viscosity was calculated using the Sutherland correlation with the coefficients defined in the ISA. The correlation accounted for the increase in viscosity with increasing temperature for low-pressure gases, where the pressure dependence could be neglected [47]. Buoyancy forces were not taken into account. The C-shaped and block-structured grids were created using Gmsh, which is an open-source 3D finite element mesh generator [48]. Systematical grid convergence studies were conducted to select suitable meshes.

4.1.1. SU2

SU2 was employed for all 2D and 3D studies. It is an open-source tool developed to solve complex, multiphysics problems [49]. Within the current study, the CFD module of version V7 "Blackbird" was used to solve FV-based RANS equations. For the reported 2D simulations, a prior mesh convergence study was conducted as per the grid convergence criteria [50] to select a mesh for further studies. For the 3D simulation cases, the effect of the propeller slipstream was modeled using an actuator disk model based on the general momentum theory with swirl and variable propeller load distribution [51].

4.1.2. OpenFOAM

The open-source CFD toolbox OpenFOAM (version v2012) was used to validate the turbulent 2D flat plate and airfoil simulations only [52]. The selected steady-state and compressible solver is based on the SIMPLE algorithm, since it is suitable for simulating turbulence and heat transfer in subsonic to transonic flow problems [52,53]. Using the Sutherland model in OpenFOAM enabled the modified Eucken correlation for polyatomic gases, which assumes a constant Pr (0.6903 for heat capacity ratio γ = 1.4) to calculate the

corresponding thermal conductivity [54]. The grid used for the parameter studies had sufficient accuracy with respect to the grid-independent solution of the aerodynamic drag coefficient, with a relative error of about 1.6%, which was calculated using the Richardson extrapolation.

4.2. Validation

The credibility of the results is based on the validation of the solver and the simulation setup against the existing literature and experimental data. The applied solvers and setups (see Section 4.1) were validated against numerical and experimental data for an adiabatic and heated flat plate, an adiabatic and partially heated NACA 0012 airfoil, and a propeller–wing configuration. All validation data is publicly available in the literature [23,55–58].

4.2.1. Flat Plate

The flat plate simulations with a zero pressure gradient were conducted for a freestream Mach number of $Ma_\infty = 0.2$, at $T_\infty = 300\,K$, and $Re_L = 5 \times 10^6$ with $L = 1\,m$. The boundary conditions were the same as for the NASA CFL3D simulations [55], which were used as validation data. Wall temperatures were uniform and constant along the length and were given as the difference between the wall and freestream temperature ΔT_w.

In Figure 5, the skin friction coefficient C_f along the plate for the adiabatic and heated wall is shown. The adiabatic SU2 and OpenFOAM simulations showed good agreement with the CFL3D simulation, although OpenFOAM led to slightly higher values. Comparing the adiabatic simulations with the incompressible correlation by White [47] indicated that the correlation overpredicted friction. Overall, heating leads to a significant reduction in frictional forces compared to the adiabatic case. Compared to OpenFOAM, the SU2 tended to slightly smaller values for both the adiabatic and heated cases. The SU2 deviated at $x = 1\,m$ by about –1.7% with respect to the heated OpenFOAM simulations.

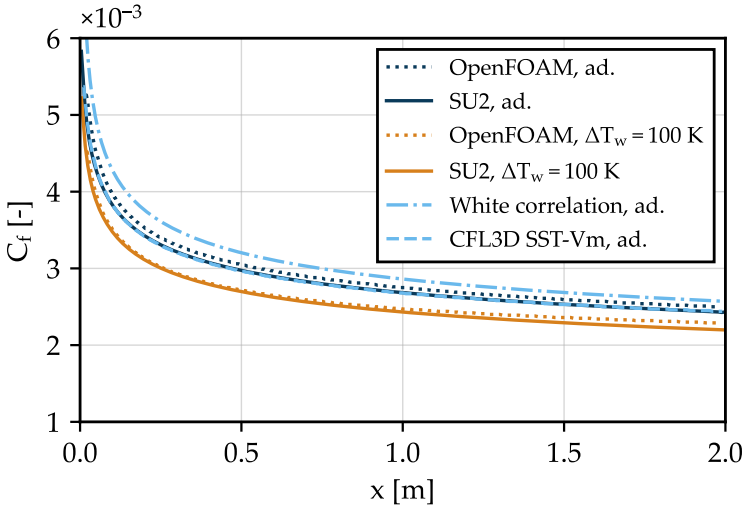

Figure 5. Skin friction coefficient C_f along the flat plate for an adiabatic and heated case with $\Delta T_w = 100\,K$ at $Ma_\infty = 0.2$, $Re_L = 5 \times 10^6$, and $T_\infty = 300\,K$.

4.2.2. NACA 0012 Airfoil

The turbulent flow over the 2D airfoil was validated against NASA's Turbulence Modelling Resource [57] data for the adiabatic conditions. For heated conditions, the laminar flow was validated against experimental data from NASA's Lewis Icing Research Tunnel (IRT) [56]. The primary objective of the heated experiments was to provide heat transfer data to be used in numerical simulations to study the ice accretion on airfoils.

For the adiabatic turbulent case, the results of the comparison of the pressure coefficient distribution C_p on the surface of the NACA 0012 airfoil are shown in Figure 6. The results of the CFL3D agreed well with the results of the SU2. In addition, the results were consistent with the Gregory experimental data [59].

For the partially heated airfoil in laminar flow conditions, the chord-length-based local Frossling number $Fr_c = \frac{Nu_c}{\sqrt{Re_c}}$ was compared. Nu_c is the chord-based local Nusselt number. The original test airfoil was fitted with an array of heat transfer gages that would maintain a constant temperature on the surface as shown in Figure 7, left. The results from the IRT for the case of the smooth airfoil (Roughness pattern: none; Spray air: off) at $\alpha \approx 2°$, $Re_c \approx 2.4 \times 10^6$ and $Ma_\infty = 0.167$ were compared against fully laminar simulation data as shown in Figure 7. The results of the 2D laminar flow simulation in the SU2 showed close agreement with the experimental Fr_c. The difference between the simulation and experiment may have been due to the 3D effects in the experiments and the stated measurement uncertainties of Fr_c at each gage of around 5% [56]. The diverging trend at $x/c \approx 0.04$ could be caused by laminar–turbulent transition, which cannot be modeled in a fully laminar numerical simulation. In addition, the turbulent simulation setup in the SU2 and OpenFOAM were compared against each other for uniformly heated NACA 0012. The result of the distribution of C_p and C_f over the airfoil surface showed consistent results, as depicted in Figure 6 for C_p.

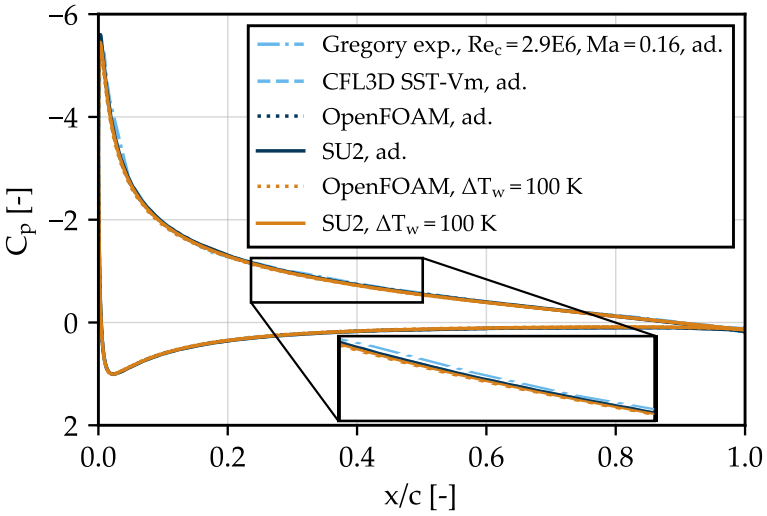

Figure 6. Pressure coefficient C_p along the NACA 0012 airfoil for an adiabatic and heated case with $\Delta T_w = 100$ K at $Ma_\infty = 0.15$, $Re_c = 6 \times 10^6$, $\alpha = 10°$, and $T_\infty = 300$ K.

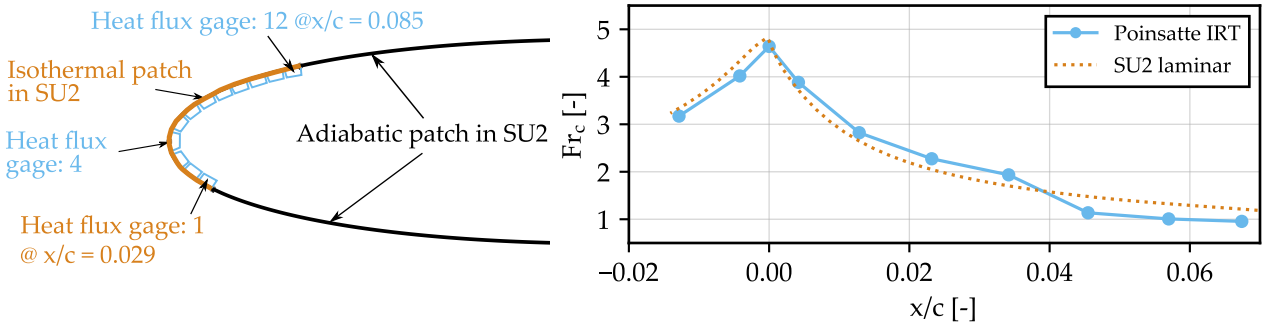

Figure 7. Cross-section of the airfoil showing position of heat flux gages in the experimental setup [56] and corresponding heat patches used in SU2 (**left**). Comparison of Fr_c for numerical and experimental data [56] (**right**).

4.2.3. Actuator Disk

The experimental test case number two, configuration "CONF 2" presented in [58,60], was simulated in the SU2 to ensure the validity of the modeling of the wing propeller interaction using Saetta's implementation of the actuator disk model with tip losses [51] (see Figure 8, left). Freestream characteristics were derived according to the experimental setup: $Ma_\infty = 0.15$, $\alpha/\beta = 0°$, $Re_c = 1.7 \times 10^6$ with $L = 0.5$ m. The turbulence intensity was assumed to be 0.25%. The properties of the actuator disk were modeled using the

geometrical data from [58]. The propeller characteristics were calculated accordingly with an advance ratio of J = 0.7.

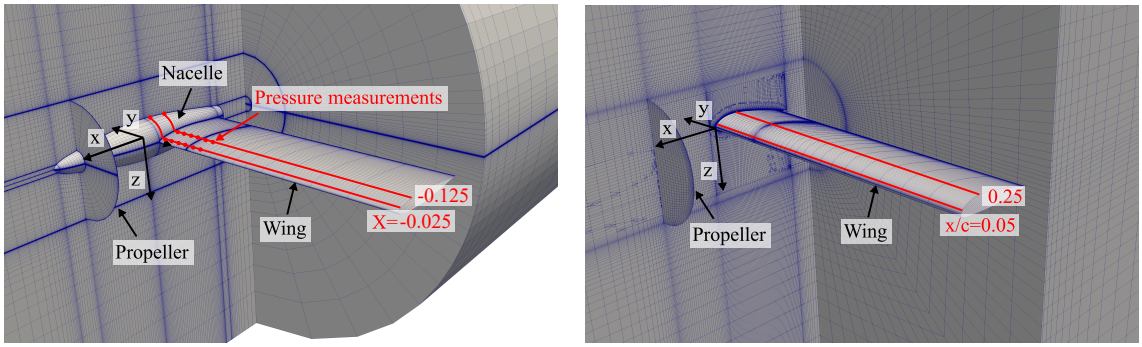

Figure 8. Visualization of the mesh for the actuator disk validation following [58] (**left**). Lines and dots indicate points of measurement. Visualization of the mesh used in the 3D study (**right**).

A comparison of exemplary simulation results against experimental data is shown in Figures 9 and 10. The simulation results of the spanwise pressure distribution agreed well with the experiments on the port side of the wing (see Figure 9). However, there was a discrepancy in the results on the starboard side. The geometry and freestream conditions were symmetric in the x-z- and x-y-plane; thus, the symmetry of ther numerical results was deemed correct under ideal conditions. It can be assumed that the experimental results were not generated under ideal conditions, because the experimental "configuration [...] is not strictly axisymmetric" as pointed out by Samuelsson in a later publication [61].

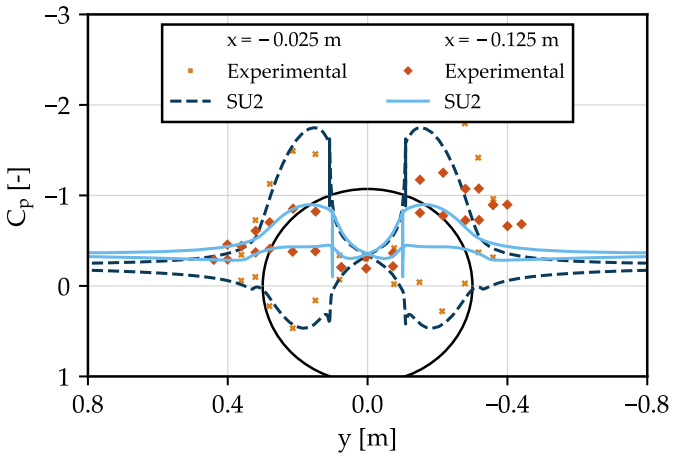

Figure 9. Spanwise pressure coefficient distribution at x = 0.025 m and x = 0.125 m downstream of the wing leading edge as indicated in Figure 8. Downstream view. Experimental data from [60].

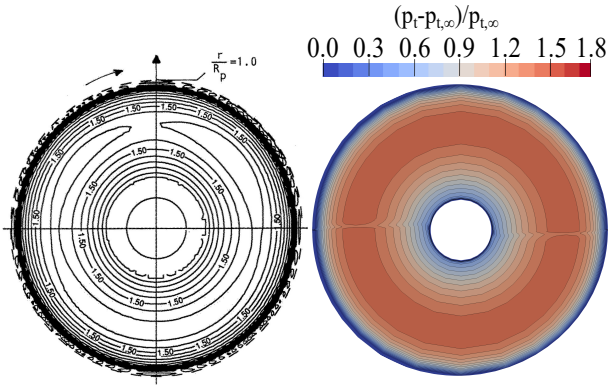

Figure 10. Total pressure distributions at x = $0.14r_{prop}$ downstream of the propeller plane. Experimental data [61] (**left**). Numerical simulation data (**right**).

The total pressure distribution behind the propeller is presented in Figure 10. Again, the results of experimental and numerical data agreed well. Due to a more detailed resolution of the numerical results, the bi-directional effect of the direction of propeller rotation on the wing was more pronounced. In addition, the swirl angle was also matched well at the same position (not shown here). In summary, the actuator disk model was deemed sufficiently accurate for the representation of the effects of propeller–wing interactions.

4.3. Study Setup

The effect of heat transfer on the aerodynamics was studied for the 2D NACA 45018 airfoil under varying ΔT_w, α, Ma_∞, and Re_c considering operating conditions of the aforementioned regional aircraft (see Table 1). The wall temperature value exploration exceeding the electrical component operating temperatures provided in Section 2.1 serve as an academic study beyond the presented application case. For the 2D case, V_∞ was considered as the propeller slipstream velocity and estimated for representative cruise conditions using axial momentum theory.

Table 1. Parameters for the 2D study of the NACA 45018 airfoil for Cruise (CR) and Take Off (TO). CR reference case marked in bold.

	h_{flight} [100 ft]	V_∞ [m/s]	ΔT_w [K]	α [°]
CR [1]	**150**	120/**140**/160/180	0/25/50/75/100/120/**140**/160/200/300	**0**
	150/160/170/180/200/220	140	140	0
	150	140	140	–5/0/+5
TO [2]	0	20/40/60/80/100	0/20/40/60/80/100/200/300	0
	0	60	0/20/40/60/80/100/200/300	0/+10

[1] ISA [2] hot day, ISA + 30.

To initially study the effect of the propeller slipstream on the heat removal potential over the wing surface, 3D simulations were carried out of an unswept inboard wing section where the propellers were located. Here, the airfoil t/c was 18%. The actuator disk emulates the properties of the six blade Hamilton Standard 568F propeller. Engine nacelles and fuselage–wing interactions were omitted in the first instance. Table 2 summarizes the study parameters. Studies were carried out for cruise conditions as well as taxi and take-off conditions, which can be critical for heat removal. The propeller thrust values corresponded to typical propeller thrusts at the studied flight conditions. The 2D grid used for the studies of the uniformly and non-uniformly heated NACA 45018 airfoil is presented in Figure 11.

Table 2. Parameters for 3D study. CR reference case marked in bold. TO: Take Off, TX: Taxi.

	h_{flight} [100ft]	Ma_∞ [-]	ΔT_w [K]	T_{prop} [kN]	α [°]
CR [1]	**200**	**0.46**	0/50/**100**	**6.5**	**0**
	200	0.46	100	8.0	0
	200	0.40	100	5.8	0
	150	0.46	100	6.5	0
TX [2]	0	0.03	0	0	0
	0	0.03	0/50	0.67	0
TO [2]	0	0.17	0	0.0	0/+10
	0	0.17	50	10.0	+10
	0	0.17	0/50	21.5	0/+10

[1] ISA [2] hot day, ISA + 30.

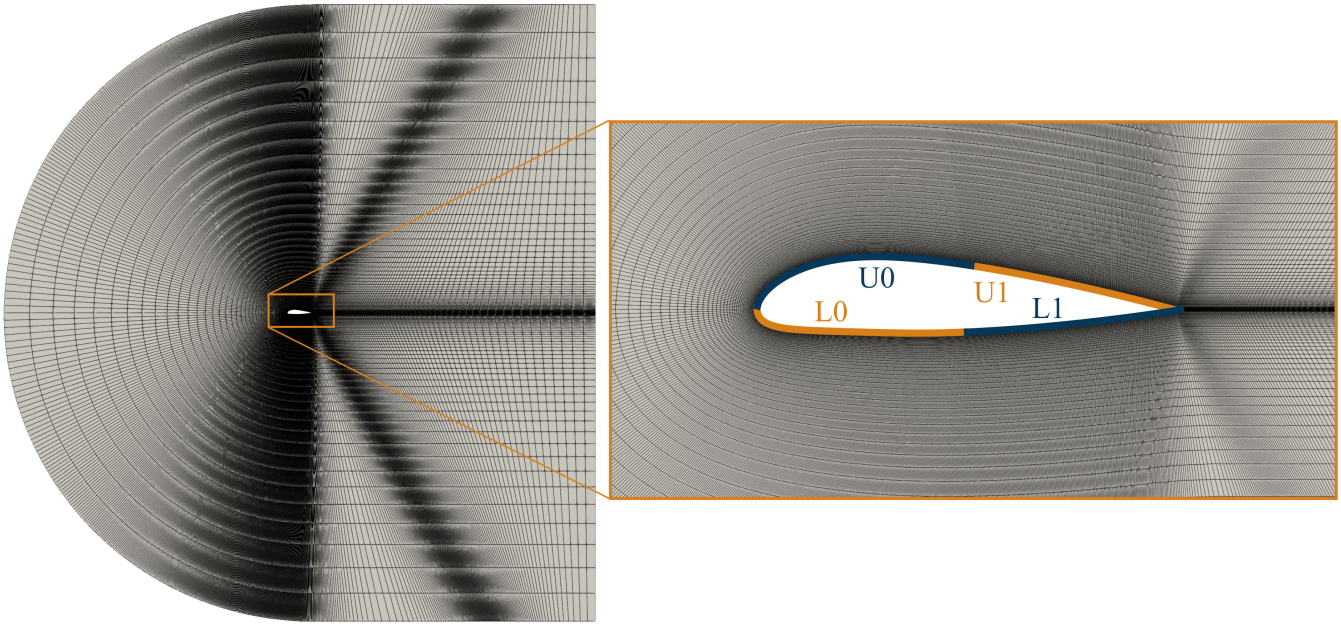

Figure 11. Visualization of the mesh used in the 2D study, including an indication of the four heat patches.

5. Uniformly Heated Two-Dimensional Airfoil

A comprehensive study of a heated NACA 45018 airfoil in turbulent freestream conditions was conducted, as well as a variation in the airfoil thickness-to-chord ratio.

In the following, Re_c, μ, and k were evaluated at film temperature $T_f = (T_w + T_\infty)/2$. k showed a linear dependency on the temperature difference under the assumption of constant Pr and specific heat c_p.

The 2D numerical results of the modified NACA 45018 airfoil indicate that sectional skin friction and pressure drag behaved opposite when the surface temperature was uniformly increased at a given Re_c. An increase in surface temperature destabilized the BL. Correspondingly, C_f decreases and flow separation were promoted, especially in cases of high α (see Figure 12). Additionally, the BL thickness increased. Both effects contributed to an increase in pressure drag with rising heat flux $\dot{q}_A$. This behavior is aligned with effects reported in the literature [20,40,44,45]. For cruise conditions, the drag coefficient C_d is reduced for small temperature differences between the airfoil surface and freestream flow for small and high α. However, for higher temperature differences, the increase in pressure drag dominates over the reduction in skin friction drag and leads to an overall drag increase, as was indicated in experiments on heated airfoils [20]. The higher the V_∞, the lower the temperature difference for which the drag coefficient reaches its minimum. In general, the drag coefficient is influenced by less than 10 drag counts for ΔT_w [0, 300] K. At the same time, the lift coefficient C_l decreased almost linearly from $\Delta T_w = 0$ K to 300 K by up to 15% (cruise conditions), which led to an overall L/D, i.e., aerodynamic efficiency and reduction in the airfoil in all flight conditions (see Figures 13 and 14). For the studied conditions and ΔT_w between 25 and 300 K, the L/D was reduced by a maximum of 14.9% in cruise ($V_\infty = 180$ m/s) and a maximum of 12.6% in take off ($V_\infty = 20$ m/s, ΔT_w between 20 and 300 K), while the average heat transfer coefficient $\bar{h}$ was reduced by 23.3% and 21.0% (Figures 13 and 14).

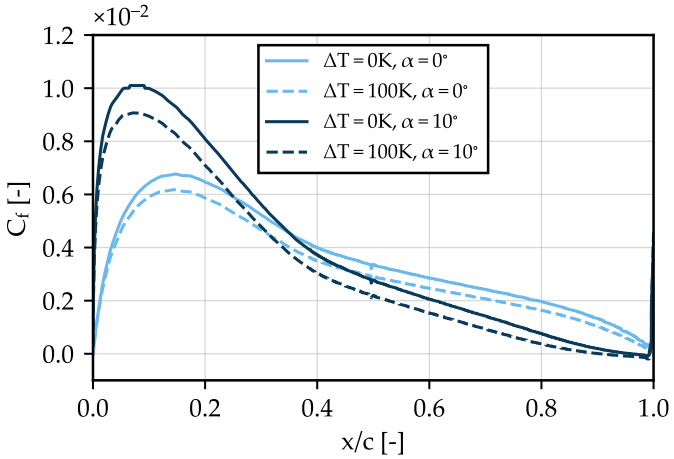

Figure 12. Skin friction distribution C_f along the top surface of the NACA 45018 airfoil at take-off conditions with V_∞ = 60 m/s. Points of flow separation (C_f = 0) are indicated.

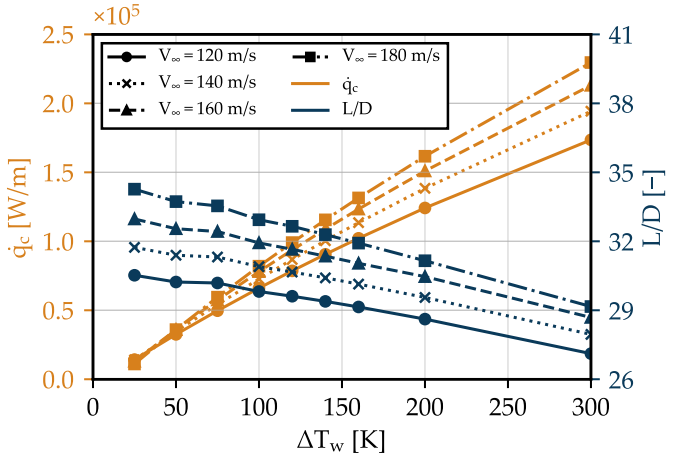

Figure 13. Chord-based heat flux $\dot{q}_c$ and lift-to-drag coefficient L/D for a variation in V_∞ and ΔT_w at h_{flight} = 15,000 ft and $\alpha = 0°$ (cruise).

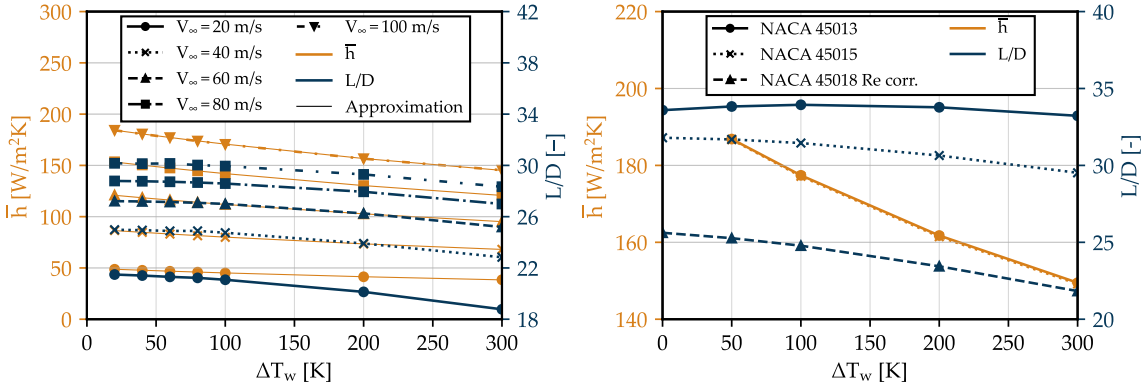

Figure 14. Average heat transfer coefficient $\bar{h}$ and lift-to-drag coefficient L/D for a variation in V_∞ and ΔT_w at h_{flight} = 0 ft and $\alpha = 0°$ (take off, **left**) and for airfoil thickness-to-chord variation at FL150, $\alpha = 0°$, V_∞ = 140 m/s and c = 1 m (cruise, **right**). Approximation: $\bar{h} = \frac{1}{c} 0.176 Re_c^{0.827} Pr^{6.453} \frac{T_\infty}{T_w}^{-0.022} k$.

Figure 15 presents an overview of the heat transfer efficiency results ($\bar{h}$ and $\overline{Nu}$) for the cruise study with a variation in V_∞ and ΔT_w for reference cruise conditions with high speeds at high altitude. The average heat transfer coefficient

$$\bar{h} = \frac{1}{2}\left(1/c \int_{x_{top}} h(x)_{top} dx + 1/c \int_{x_{bottom}} h(x)_{bottom} dx\right)$$

and the average Nusselt number $\overline{Nu} = \frac{\bar{h}L}{k}$ are related to ΔT_w and Re_c, respectively. The results of the numerical study were compared against correlations for a flat plate, which was valid for 1e7 < Re_L < 1e9 and 0.6 < Pr < 15:

$$\overline{Nu_L} = 0.185 \frac{Re_L Pr^{1/3}}{(\log_{10} Re_L)^{2.584}}$$

Ref. [62] and the Churchill–Bernstein correlation for a cylinder in cross-flow for $PrRe_D > 0.2$ and Re_D > 4e5:

$$\overline{Nu_D} = 0.3 + \frac{0.62 Re_D{}^{0.5} Pr^{1/3}}{(1 + (\frac{0.4}{Pr})^{2/3})^{1/4}} \left[1 + \left(\frac{Re_D{}^{1/2}}{282,000}\right)^{5/8}\right]^{4/5}$$

Ref. [63]. In addition, numerical data were compared against a modified version of the Hilpert correlation for cylinders in cross-flow, which is often used to characterize the heat transfer efficiency of airfoils but is valid only for 4e4 < Re_D < 4e5

$$\overline{Nu_D} = 0.027 Re_D{}^{0.805} Pr^{1/3} \quad (1)$$

Refs. [64,65].

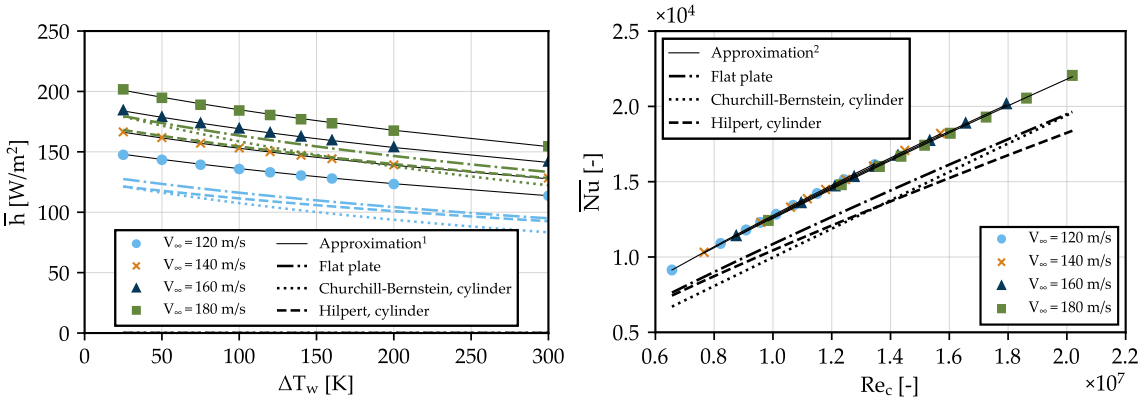

Figure 15. Average heat transfer coefficient $\bar{h}$ (**left**) and average Nusselt number $\overline{Nu}$ (**right**) for a variation in V_∞ and ΔT_w at h_{flight} = 15,000 ft and $\alpha = 0°$ compared against correlations for a flat plate [62] and for circular cylinders in cross-flow [63,64]. Approximation^1: $\bar{h} = \frac{\overline{Nu}}{c}$; Approximation^2: $\overline{Nu} = 0.385 Re_c^{0.755} Pr^{5.285} \frac{T_\infty}{T_w}^{0.044} k$.

In all cases, the chord length of the airfoil was taken as the reference length and Pr was constant. The trend of the simulation results for $\bar{h}$ followed the trend of the correlations, while the absolute values were generally higher. The smallest difference between simulation data and empirical correlation occurred for the flat plate correlation. Here, the maximum difference was 16.0% for V_∞ = 120 m/s and 19.7% for V_∞ = 180 m/s.

An approximation with a non-linear least squares curve fitting approach of the dependency of $\bar{h}$ and $\overline{Nu}$ on the Re_c, Pr, and T_∞/T_w that was similar to [41] led to the approximations given in Figure 15 with a coefficient of determination of R^2 = 0.9998. In addition, the $\overline{Nu}$ in relation to the Re_c followed a trend that has been previously observed in the characterization of airfoils in other studies [65].

For each V_∞, the film effectiveness, represented by the heat transfer coefficient, was optimal for the lowest temperature difference (Figure 15). For higher temperature differences, the heat transfer coefficient decreased with increasing ΔT_w. In this region, the increase in chord-based heat flux

$$\dot{q}_c = 1/c \int_{x_{top}} \dot{q}_{A,top}(x)dx + 1/c \int_{x_{bottom}} \dot{q}_{A,bottom}(x)dx$$

was smaller compared to the rise in T_f (see Figure 13). In general, the total rejected heat increased with increasing ΔT_w and V_∞ (see Figure 13).

A similar behavior can be observed for lower speeds at a lower altitude (take off) in Figure 14. Here, the approximation of $\overline{h}$ had an $R^2 = 0.9999$.

A variation in α showed a similar trend (Figure 16, left). At $\alpha = 5°$, the L/D decreased faster with increasing ΔT_w compared to $\alpha = 0°$. The $\overline{h}$, however, followed a similar trend for all α. On the top side of the airfoil, the heat flux was lower than on the bottom side for $\alpha = 0°$. For $\alpha = 5°$, the heat flux on the lower side increased significantly less than it rose on the upper side and, thus, the $\overline{h}$ was reduced. This result aligns with experimental airfoil results obtained by Wang et al., who found that, for a moderate increase in α, the $\overline{Nu}$ and $\overline{h}$ can be reduced [19]. The opposite occurs for the negative α. Here, the reduction in heat flux on the suction and the increase on the pressure side compensated each other, and, hence, the $\overline{h}$ remained unchanged compared to $\alpha = 0°$. For high α, heat rejection can foster destabilization of the BL and lead to a further increase in drag partly due to flow separation as shown for take-off conditions (see Figure 12).

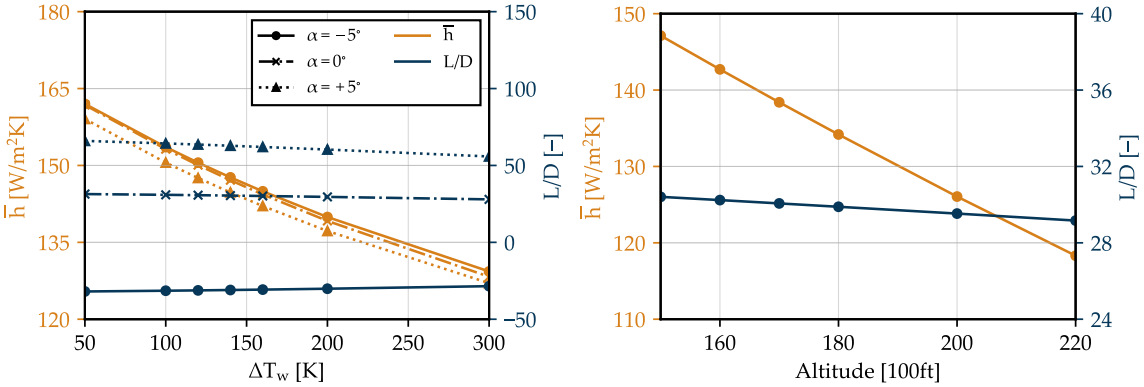

Figure 16. Effect of angle of attack variation at $V_\infty = 140\,m/s$ and $h_{flight} = 15,000$ ft (**left**) and flight level variation at $V_\infty = 140\,m/s$ and $\alpha = 0°$ (**right**) on average heat transfer coefficient $\overline{h}$.

As pictured in Figure 16, the dependency of the L/D and $\overline{h}$ on flight altitude h_{flight} was purely driven by the fluid's freestream characteristics, mainly by the k and Re_c. At higher altitudes, the aerodynamic performance decreased by 4% for the studied parameter range, while the $\overline{h}$ deteriorated by almost 20%.

It can be concluded that uniformly rejecting heat via 2D airfoils in turbulent flow conditions leads to a degradation of the aerodynamic performance of the airfoil, independent of the flight conditions. At the same time, the heat transfer coefficient was reduced. Empirical correlations for the heat transfer efficiency of the flat plates or circular cylinders in cross-flow can be modified to model the characteristics of the studied airfoil. Thus, it is important to characterize the aerodynamic performance of particular airfoils with respect to their heat rejection characteristics in order to evaluate the impact of heat rejection over a WSHX meaningfully.

At the wing tips, the maximum t/c of the airfoils was smaller compared to the wing root. To initially explore the effect of surface heating on airfoils with a smaller t/c, numerical simulations were carried out for the NACA 45013 and NACA 45015 airfoils with t/c = 13 and 15% (see Figure 2) and a chord length of c = 1 m. The L/D was compared against results of the NACA 45018 airfoil, which were corrected to match the Reynolds number.

The t/c variation of the five-digit NACA airfoils showed a high dependency of the L/D variation caused by surface heating on the shape of the airfoil (Figure 14, right). For the unheated case ($\Delta T_w = 0\,K$), the L/D increased with decreasing t/c. For the 13% airfoil, surface heating positively affected the lift-to-drag ratio, with a L/D optimum for $\Delta T_w \approx 100\,K$, which was ≈1% higher than for the unheated case. The bigger t/c, the worse the effect of heating on the aerodynamic performance of the airfoil. For a maximum temperature difference of $\Delta T_w = 300\,K$, the L/D of the NACA 45015 and NACA 45018

airfoil decreased by 7% and 15%, respectively. The high curvature of the NACA 45018 leading edge promoted a faster development of the BL thickness and a more pronounced interaction of locations with high absolute pressure and the BL, especially on the suction side of the airfoil. The Re_c correction could not be applied to the heat transfer efficiency. Thus, only results for the NACA 45013 and NACA 45015 airfoil are presented in Figure 14. For the same Re_c, different t/c affected the $\bar{h}$ only insignificantly. The influence of surface heating showed a similar trend compared against results of the NACA 45018 airfoil in a different Re_c regime.

6. Heat Patches on a Two-Dimensional Airfoil

To investigate the effects of non-uniform heating, the NACA 45018 airfoil was divided into four sections as shown in Figure 11. The simulations were compared at cruise conditions and at ΔT_w = 140 K.

The L/D increased by 5.1% and 4.6%, respectively, compared to the unheated case for the two patches, L0 and L1, on the lower side of the airfoil. For the upper patches, U0 and U1, a decrease in the L/D by 7.0% and 6.5%, respectively, compared to the unheated case was indicated, while the uniformly heated case showed a deterioration of about 4.3%.

The lift coefficient followed the same trend. Heating the lower patches, L0 and L1, slowed down the flow over the lower surface due to an increase in the viscosity of the air in the vicinity of the surface and an increase in the boundary layer thickness. This resulted in a higher positive pressure on the pressure side, which was favorable for a higher lift. The same effect could be observed for the cases U0 and U1; however, a higher positive pressure on the suction side of the airfoil resulted in a lift decrease. Since the heating decreased the local C_f, the drag coefficient decreased for the heated cases. Due to the direction of the flow, heating upstream patches (U0, L0) resulted in the reduction of skin friction on the downstream patches (L1, U1), while heating downstream patches (U1 and L1) did not affect the upstream patches. The reduction in C_d compared to unheated case for the L0, L1, U0, and U1 cases were 2.1%, 0.95%, 0.77%, and 0.26%, respectively. Similar to results presented in the literature, the best heat patch location for drag reduction was close to the leading edge on the pressure side [23,66].

In summary, results indicate that rejecting heat only via the pressure side of the airfoil can reduce airfoil drag without promoting flow separation on the upper surface of the airfoil, especially at high angles of attack during a take-off or landing approach (Figure 17).

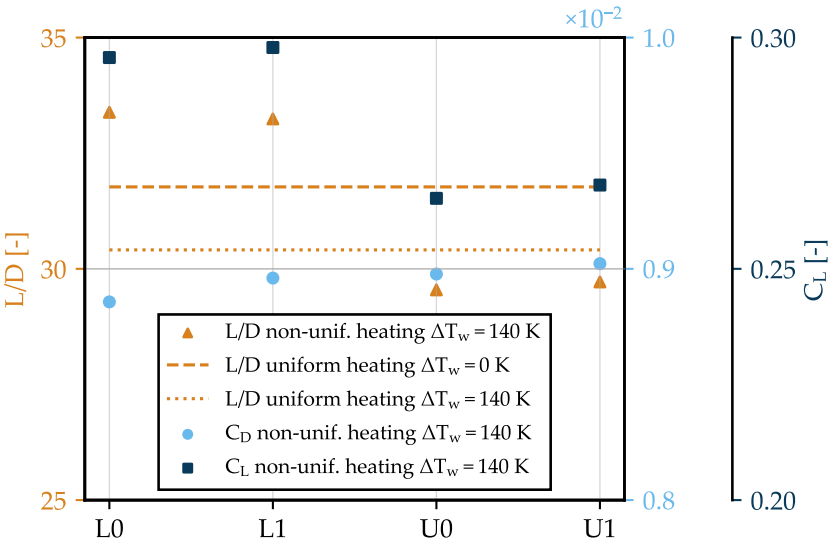

Figure 17. Lift-to-drag ratio, as well as drag and lift coefficient for heated patches at FL150; $\alpha = 0°$ and V_∞ = 140 m/s compared against uniformly heated airfoils at same flight conditions.

7. Uniformly Heated Three-Dimensional Unswept Wing Section

The effect of propeller slipstream on the heat rejection potential of a simplified WSHX was analyzed for a 3D simulation case with an actuator disk as depicted in Figure 8 (right).

Due to the asymmetry of the NACA 45018 airfoil and the low z position of the actuator disk (center of the actuator disk 0.52 m below the wing leading edge, see Figure 8, right), the effect of the propeller slipstream on the spanwise flow characteristics was asymmetrical, as depicted for a cruise case in Figure 18. Furthermore, the influence of the propeller was highest within the propeller plane and did not extend far in the spanwise direction, especially for C_f and $\dot{q}_c$. Since the propeller rotates counter-clockwise when looking upstream, the impact of its swirl on the suction and pressure sides of the wing was opposite.

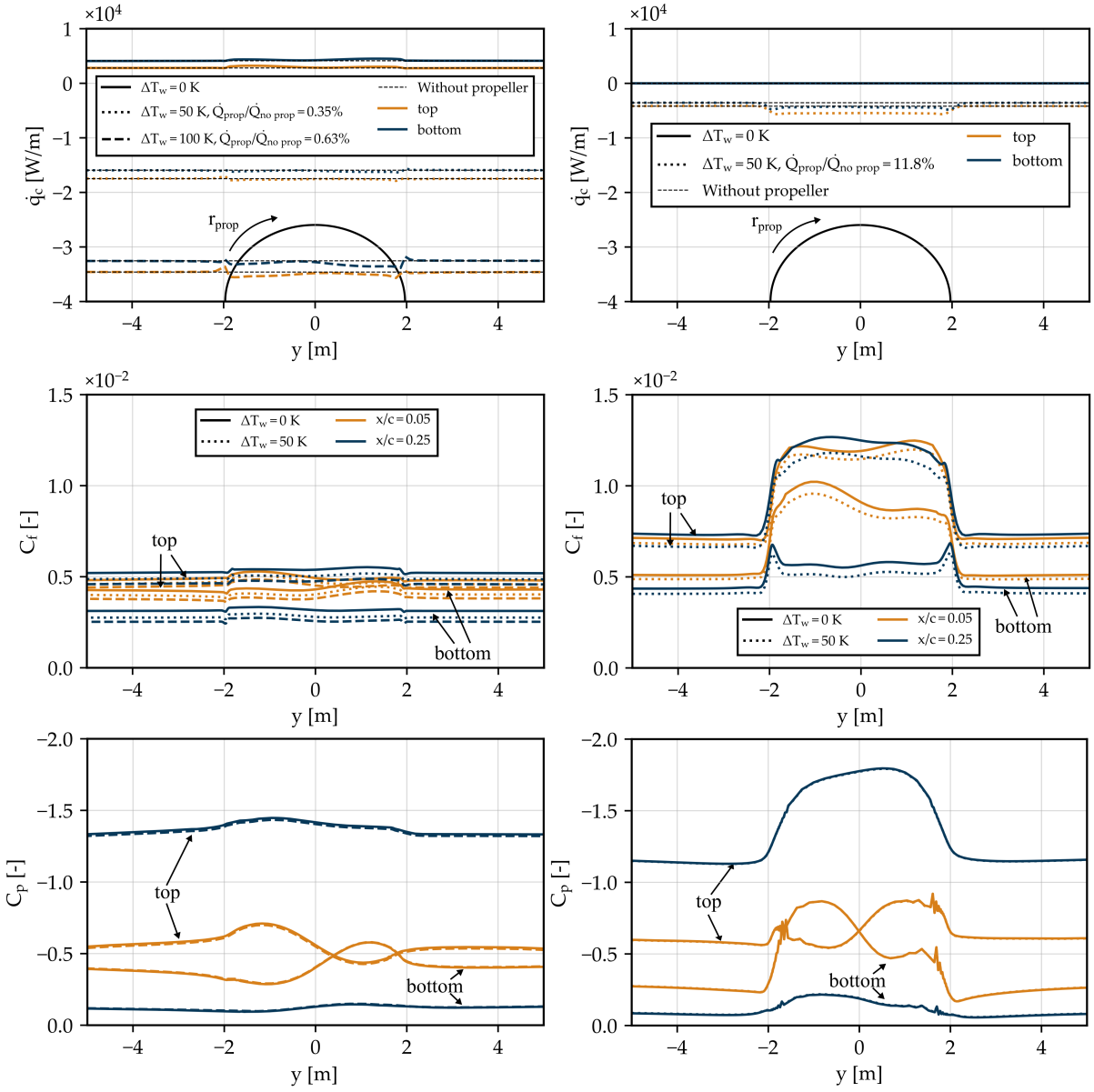

Figure 18. Exemplary spanwise C_f, C_p, and chord-length based heat flux $\dot{q}_c$ distribution at cruise conditions with FL200; Ma_∞= 0.46 and T_{prop} = 6.5 kN (**left**) at taxi conditions with Ma_∞= 0.03 and T_{prop} = 0.7 kN (**right**) for wing surface temperature variation. Downstream view. Propeller rotates in counter-clockwise direction.

In general, C_f decreased on both sides of the airfoil with increasing ΔT_w. The absolute reduction in C_f was almost constant along the span, but increased along the chord length in the front part of the airfoil as pictured exemplary in Figure 19.

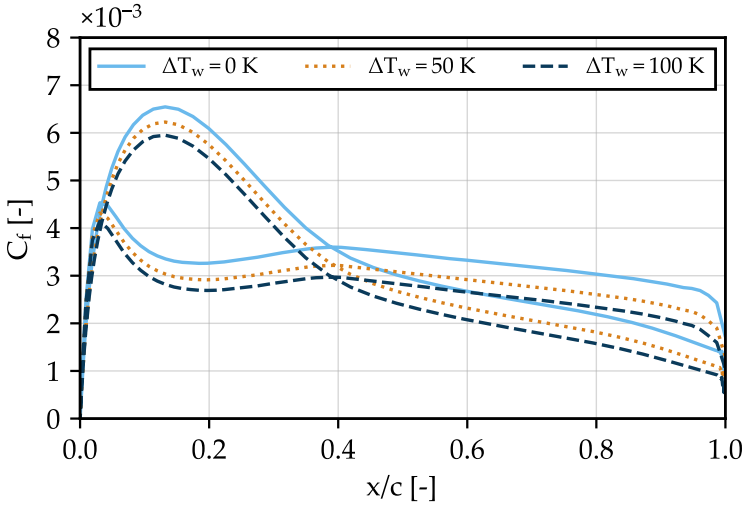

Figure 19. Exemplary chordwise skin friction coefficient C_f distribution at FL200, Ma_∞= 0.46 and T_{prop} = 6.5 kN for wing surface temperature variation at y = 1.2 m.

The influence of the propeller slipstream on the spanwise C_p was aligned with the results for the wing–propeller validation case presented in Section 4.2.3. On starboard, the upward movement of the modeled propeller blades led to an increased suction on the upper side of the airfoil, while pressure rose on the lower side, which could be compared to a local α alteration. The effect was reversed on the port side where the propeller blades move downwards.

For all studied flight conditions, the effect of surface heating on the spanwise C_p distribution was small in comparison to the influence of the propeller on the fluid characteristics.

In the following, the effects of heating are explained in detail for the different flight conditions.

In cruise conditions, a small pressure decrease on the pressure side and an increase on the suction side of the wing for rising surface temperatures led to a C_L decrease of ≈2% between ΔT_w = 0 and 100 K. At the same time, the significant impact of heating on the C_f caused an overall C_D reduction of ≈3%, which eventually resulted in a rise in the L/D of ≈1%. Thus, compared to the 2D sectional airfoil, the L/D of the 3D wing could be slightly improved when heat was rejected via the wing surface at small ΔT_w.

The propeller slipstream had a bigger influence on the heat flux in the spanwise direction for higher temperature differences. For ΔT_w = 0 K, $\dot{q}_c$ was bigger than zero, because if the surface temperature equals the freestream temperature, the wall temperature is smaller than the adiabatic temperature for which heat flux is zero by definition.

Compared to a wing, which is not under the influence of a propeller slipstream, the total heat transfer $\dot{Q} = \int_x \int_y (\dot{q}_{bottom}(x) + \dot{q}_{top}(x))dxdy$ could only be increased by up to $\Delta\dot{Q}/\dot{Q}_{no\ prop} = \frac{\dot{Q}_{prop} - \dot{Q}_{no\ prop}}{\dot{Q}_{no\ prop}}$ = 0.63% for the presented wing section of 10 m span (see Figure 18, left).

When increasing the propeller thrust from 6.5 to 8.0 kN (modeled by radial actuator disk thrust and power coefficient distribution), the L/D decreased only minorly. The variation in C_p is also insignificant. However, especially near the trailing edge of the wing, an increased C_f for increased thrust was accompanied by a rise in $\dot{q}_c$ due to higher local flow velocities.

Because of the combined Ma_∞ and T_{prop} variation, results for the aerodynamic behavior of the wing in cruise conditions did not match the results for the pure freestream velocity variation of the 2D airfoil study presented in Section 5. In accordance with the

2D airfoil results, the C_f increased with decreasing freestream Ma_∞, while the negative C_p locally decreased in the front part of the airfoil. This effect was further enhanced by the thrust variation. Consequently, in contrast to the isolated velocity variation studied for the 2D airfoil, the L/D was higher for smaller velocities, because the influence of the skin friction reduction on the drag reduction was significantly higher than the influence of the pressure force reduction on C_L.

Results for the cruise altitude variation were in agreement with the results discussed for the 2D airfoil. Along the whole wingspan and chord length, the skin friction drag reduced with increasing flight level; the pressure drag rose only minorly, leading to an overall L/D deterioration. At the same time, the heat flux was reduced. In combination with the corresponding fluid characteristics, the $\bar{h}$ decreased.

Taxi in can be a critical condition for the design of the TMS due to an unfavorable combination of a low freestream velocity incident to the WSHX, a low propeller thrust, and high excessive waste heat loads.

The propeller induced momentum led to an increase in the area averaged velocity inside the propeller slipstream by 35% compared to the freestream velocity at $x/c = 0.25$. In consequence, the propeller-assisted forced convection in the propeller slipstream increased the area-based heat flux $\dot{q}_A$ inside the propeller slipstream by almost 29%. This led to a rise in the total heat transfer potential by almost 12% over the depicted span of 10 m (see Figure 18, right). However, the absolute available heat transfer in taxi was <25% of the available heat transfer in take off or cruise. Consequently, the total available heat transfer capacity in taxi stayed small. Aerodynamic drag decreased by 1% when the surface temperature increased by $\Delta T = 50$ K from the freestream temperature. Thus, heating slightly improved the the aerodynamic efficiency in taxi.

During take-off rotation, the aircraft rotated around its pitch axis. For the investigated aircraft, a maximum pitch angle of 10° was analyzed. Independent of thrust and ΔT_w, increasing α caused a significant increase in C_p, which resulted in a C_D and C_L rise. As the lift was affected less compared to drag, the L/D was reduced by more than 20%.

For $\alpha = 10°$, $\Delta T_w = 50$ K, and $T_{prop} = 21.5$ kN, the $\dot{Q}$ was ≈32% higher compared to the same case with $\alpha = 0°$. This effect was directly connected to the pressure rise as elaborated in Section 5.

The area-averaged Mach number in the propeller slipstream in front of the wing leading edge increased proportionally with propeller thrust. Consequently, $\dot{Q}$ rose. For $\Delta T_w = 50$ K, $T_{prop} = 10.0$ kN, and $\alpha = 10°$, 13% more heat could be transferred over the wing surface, which was affected by the slipstream, compared to the same case without a propeller (see Figure 20). When T_{prop} was increased to 21.5 kN, $\Delta\dot{Q}/\dot{Q}_{no\ prop} = 20\%$ in the slipstream area.

The aerodynamic efficiency of the wing for the given take-off conditions deteriorated when heat was rejected over the surface. As the interaction of the propeller slipstream and wing was strong for this condition, the reason for this differed for $\alpha = 0°$ and 10°.

For the take-off case with $\alpha = 0°$, the L/D deteriorated by 0.2% when the surface temperature was increased by 50 K. This was caused by a combination of a rise in pressure drag and a decrease in viscous drag and lift (Figure 20, left).

For $\alpha = 10°$, the L/D reduced by 3.8% as pressure drag increased and lift decreased. At the same time, friction drag rose, because the skin friction coefficient increases along the whole chord length of the lower wing surface, while it decreased at the front part of the upper surfaces and increased near the trailing edge (see Figure 20, right). In all cases, no flow separation occurred. For $\alpha = 10°$, pressure drag contributed to up to 87.4% of the total drag and, thus, had a bigger impact on the wing aerodynamic efficiency compared to the drag attributed to skin friction.

In conclusion, numerical 3D results indicate that the accelerated air in the propeller slipstream has a beneficial effect on the heat transfer capability of a wing in representative flight conditions. At the same time, the wing L/D is not affected in a negative way when

increasing ΔT_w for cruise conditions. In take off, however, the aerodynamic performance deteriorated by up to 3.8% during rotation.

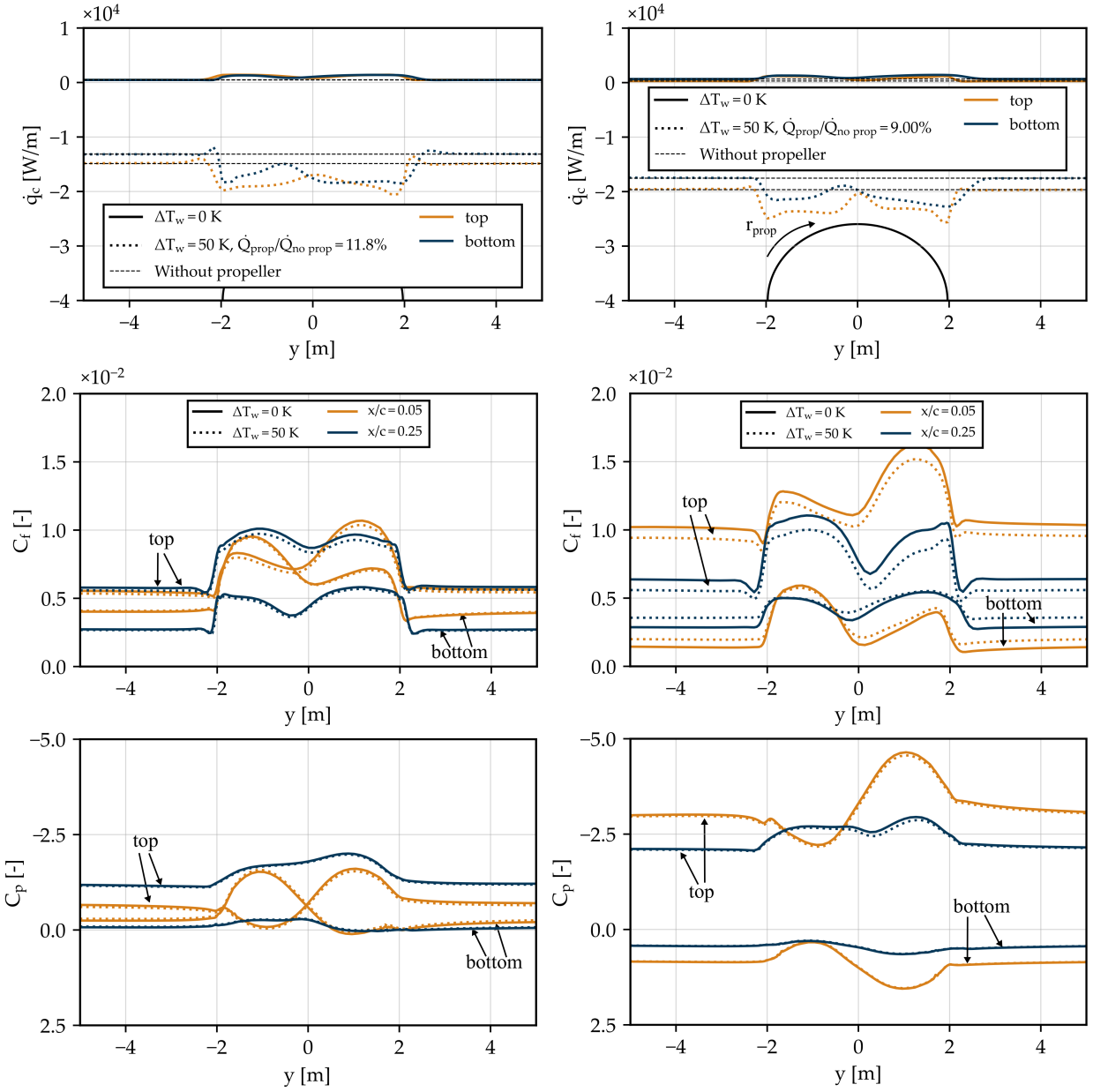

Figure 20. Exemplary spanwise C_f, C_p and chord-length-based heat flux $\dot{q}_c$ distribution at take-off conditions with Ma_∞= 0.17, T_{prop} = 21.5 kN, α = 0° (**left**) and α = 10° (**right**) for wing surface temperature variation. Downstream view. Propeller rotates in counter-clockwise direction.

8. Conceptual Aircraft Design Implications

For a holistic analysis of the synergistic effects of a WSHX with a HEP aircraft configuration, the isolated numerical results of the presented study will be integrated in the multi-disciplinary aircraft design of the IMOTHEP REG-CON configuration. It will be studied if the WSHX concept has a beneficial effect on the aircraft level in comparison to a conventional ram air TMS when taking into account all implications on system weight, aerodynamic efficiency, and heat transfer efficiency of the wing in all flight conditions [67]. A focus will be placed on flight conditions for which sufficient heat rejection is challenging due to a combination of high heat loads, small temperature differences between wing surface, and the ambient and reduced fluid velocity, such as for taxi-in or take-off conditions [10].

Here, the strategical usage of certain areas of the wing for heat rejection will be considered. The t/c variation shows that rejecting heat via airfoils with a smaller t/c (for this particular airfoil and cruise flight conditions), can be beneficial for the aerodynamic performance of the airfoil. Even though the REG-CON concept foresees dissipating heat primarily in the vicinity of the propeller slipstream, it might be beneficial to investigate the potential of rejecting heat along the whole wing span, especially in critical flight conditions.

For a realistic application case of a WSHX, the wing will also not be heated uniformly along the chord length. From an aerodynamic perspective, it is beneficial to heat the leading edge of the airfoil. However, in a more practical scenario, fuel circulating through the wing tanks located in the center section of the wing in the chordwise direction could be used as a coolant to transfer the heat from the electrical components to the aircraft's surface. If the excessive waste heat is rejected via the fuel stored in the wing tanks, then, in most flight phases, heat will mainly be rejected through the lower side of the wing. This is caused by the low thermal conductivity of the air layer between the fuel and upper wing surface inside the tank, which decreases heat transfer to the upper side of the wing [10].

The 3D numerical simulations of a wing section under the influence of the propeller slipstream indicate a small improvement of the aerodynamic efficiency of the wing when heat is rejected via its surface at cruise conditions. During taxi-in conditions, the aerodynamic drag is small compared to the rolling friction of the aircraft's tiers [68]. Thus, for taxi conditions, the effect of surface heating on the aerodynamic performance is irrelevant. Furthermore, it can be expected that the waste heat, which has to be rejected in taxi conditions, is small, because the required propulsive power is small during this flight phase. During the take-off phase, the highest propulsive power demands can be expected. Here, the highest excessive waste heat rates have to be rejected.

In general, the turboprop configuration seems to be a suitable aircraft configuration for a WSHX, because heat flux across the wing surface is significantly increased by the propeller slipstream.

However, a detailed TMS and aircraft design analysis has to prove if the available heat transfer rate is sufficient in all flight phases to reject the excessive waste heat contributed to the electrical components of the HEP aircraft. Otherwise, a combination of a WSHX with a conventional ram air TMS has to be considered.

9. Conclusions

The emission reduction potential of a regional HEP aircraft configurations is partially dependent on the efficient rejection of excessive heat loads caused by the electrical components required to propel the aircraft. To foster a better understanding of first and second order effects of the specified heat exchanger concept on aircraft level, the presented study investigated the aerodynamic and heat transfer efficiency of a WSHX. The 2D RANS CFD results showed that the effect of heating an airfoil on its heat transfer characteristics can be represented with sufficient accuracy by modified existing empirical correlations. For the investigated NACA 45018 airfoil in cruise conditions, the following equation was derived

$$\overline{h} = \frac{1}{c} 0.176 Re_c^{0.827} Pr^{6.453} \left(\frac{T_\infty}{T_w}\right)^{-0.022} k$$

For take-off conditions, the relationship is

$$\overline{h} = \frac{1}{c} 0.385 Re_c^{0.755} Pr^{5.285} \left(\frac{T_\infty}{T_w}\right)^{0.044} k$$

The correlations have to be adapted based on the aerodynamic and heat transfer characteristics of the specific airfoil, which can be derived from experiments or numerical simulations. The average airfoil heat transfer coefficient degradation is bigger than a minor decrease in aerodynamic efficiency represented by the L/D. This holds true for flight conditions representative for cruise as well as take off. Increasing ΔT_w from 25 to

300 K resulted in an L/D degradation of up to 15% and an average heat transfer coefficient reduction of up to 23% for cruise conditions.

However, high angles of attack, which occur during take off at small altitudes and flight velocities, can lead to an increase in BL instability accompanied by an earlier onset of flow separation on the suction side of the airfoil and a significant rise in sectional drag. For the studied conditions, the point of flow separation moved upstream by a 6% chord fraction when increasing the wall temperature by 100 K at $\alpha = 10°$.

For high freestream velocities and flight altitudes, the impact of the propeller slipstream is small and in the same range for both the amount of heat, which can be rejected via the wing surface, and the aerodynamic efficiency. Here, the total heat transfer was improved by less than 1%. For flight phases for which the amount of heat generated by the electrical components is high and the heat removal potential of the wing without propeller is low, such as a hot day, take off, or taxi in, the effect of the propeller slipstream on the heat rejection potential is more significant (up to 12% depending on freestream conditions and propeller thrust).

For a better understanding of the effect of heat rejection via the wing surface, additional numerical studies should be conducted in the future. In a next step, a full wing geometry should be studied, including varying airfoil t/c in the spanwise direction, wing sweep, and dihedral. Eventually, it should be investigated how the interaction of wing, engine nacelle, belly-fairing and fuselage affects the heat rejection potential of the wing. Based on the results for non-uniform airfoil heating, it might be promising to investigate the rejection of heat at strategic locations of the wing, such as the leading edge (for aircraft without leading edge devices) or the wing fuel tank. Here, heat is mostly rejected through the lower side of the wing. Furthermore, it needs to be studied how the high-lift configuration of the wing (compared to the studied clean wing configuration) affects its heat transfer potential and aerodynamic performance in take-off conditions. The accuracy of the presented results calculated with a steady RANS solver is deemed promising due to the accurate prediction of the experimental validation data. Even though k-ω-SST turbulence models are well suited to predict the onset of separated turbulent regions [69], RANS solvers are not very reliable for predicting the flow inside these regions [70]. Here, the flow is not necessarily in equilibrium and is governed by unsteady length and time scales [71]. Thus, turbulence models employed in RANS simulations tend to underestimate turbulent shear stress and turbulence kinetic energy within separated turbulent regions, thus leading to inaccurate predictions of the flow behavior [72]. For most investigated flow conditions, no separation occurred. However, especially in take-off conditions at $\alpha > 0°$, the accuracy of the results might not be maintained. To obtain more accurate predictions of these separated flows, more advanced CFD methods, such as Large Eddy Simulation (LES) or Direct Numerical Simulation (DNS), may be required. These methods can capture the unsteady and turbulent nature of the flow behavior in separated regions with a higher accuracy [71].

Finally, the numerical results should be validated against corresponding wind tunnel experiments.

To understand the implications of a WSHX on the aircraft's performance from an aircraft level perspective, the results of the presented study will be included in an integrated aircraft design as part of the IMOTHEP project. The results will be used to identify which TMS (conventional ram drag or surface heat exchanger) has a more beneficial effect on mission fuel burn for the specified HEP aircraft configuration [31,67].

In summary, the numerical results of the present initial study indicate that it is beneficial to employ the propeller slipstream to increase the heat transfer potential in critical flight conditions. It was shown that rejecting excessive waste heat via the wing of a regional turboprop configuration can have a negative but not a detrimental effect on the wing's aerodynamics. Thus, from an aerodynamic perspective, a WSHX could be a feasible concept to reject heat even in crucial flight conditions, such as take off or taxi in, in which convection can be forced by the propeller slipstream downstream of the propeller plane.

Author Contributions: Conceptualization, A.L.H.; methodology, A.L.H., A.K., D.E.L. and C.P.; validation, A.K., D.E.L. and C.P.; formal analysis, A.L.H., A.K., D.E.L. and C.P.; investigation, A.L.H., A.K., D.E.L. and C.P.; data curation, A.L.H.; writing—original draft preparation, A.L.H., A.K., D.E.L. and C.P.; writing—review and editing, A.L.H., A.K., D.E.L. and C.P.; visualization, A.L.H., A.K., D.E.L. and C.P.; supervision, A.L.H. All authors have read and agreed to the published version of the manuscript.

Funding: This project has received funding from the European Union's Horizon 2020 research and innovation programme under grant agreement No 875006 IMOTHEP.

Institutional Review Board Statement: Not applicable.

Informed Consent Statement: Not applicable.

Data Availability Statement: Not applicable.

Acknowledgments: We thank Hagen Kellermann for their expertise and useful discussions.

Conflicts of Interest: The authors declare no conflict of interest.

Abbreviations

The following abbreviations are used in this manuscript:

BL	Boundary Layer
CFD	Computational Fluid Dynamics
CR	CRuise
FV	Finite Volume
HEP	Hybrid-Electric Propulsion
IMOTHEP	Investigation and Maturation of Technologies for Hybrid Electric Propulsion
IRT	Icing Research Tunnel
ISA	International Standard Atmosphere
MSES	Software for High Lift Multielement Airfoil Configurations)
NACA	National Advisory Committee for Aeronautics
NASA	National Aeronautics and Space Administration
PI	Point of Inflection
PaWAT	Preliminary Design Tool for Propeller–Wing Aerodynamics
RANS	Reynolds-Averaged Navier Stokes
REG-CON	REGional CONservative
TMS	Thermal Management System
TO	Take-Off
TX	Taxi
WSHX	Wing Surface Heat Exchanger

References and Notes

1. *Aircraft Electrical Propulsion—Onwards and Upwards;* Technical Report; Roland Berger: London, UK, 2018.
2. Brelje, B.J.; Martins, J.R. Electric, hybrid, and turboelectric fixed-wing aircraft: A review of concepts, models, and design approaches. *Prog. Aerosp. Sci.* **2019**, *104*, 1–19. [CrossRef]
3. Isikveren, A.T.; Seitz, A.; Vratny, P.C.; Pornet, C.; Ploetner, K.O.; Hornung, M. Conceptual Studies of Universally-Electric Systems Architectures Suitable for Transport Aircraft. In Proceedings of the 61. Deutscher Luft- und Raumfahrtkongress (DLRK), Berlin, Germany, 11 September 2012; Deutsche Gesellschaft für Luft- und Raumfahrt, Ed.; DLRK: Berlin, Germany, 2012.
4. Kuhn, H.; Seitz, A.; Lorenz, L.; Isikveren, A.T.; Sizmann, A. Progress and perspectives of electric air transport. In Proceedings of the 28th Congress of the International Council of the Aeronautical Sciences, Brisbane, Australia, 23–28 September 2012; International Council of the Aeronautical Sciences: Bonn, Germany, 2012; pp. 4886–4899. [CrossRef]
5. Pornet, C.; Gologan, C.; Vratny, P.C.; Seitz, A.; Schmitz, O.; Isikveren, A.T.; Hornung, M. Methodology for Sizing and Performance Assessment of Hybrid Energy Aircraft. *J. Aircr.* **2015**, *52*, 341–352. [CrossRef]
6. Stoll, A.M.; Veble Mikic, G. Design Studies of Thin-Haul Commuter Aircraft with Distributed Electric Propulsion. In Proceedings of the 16th AIAA Aviation Technology, Integration, and Operations Conference, Washington, DC, USA, 13–17 June 2016.
7. McCluskey, P.; Saadon, Y.; Yao, Z.; Shah, J.; Kizito, J. Thermal Management Challenges in Turbo-Electric and Hybrid Electric Propulsion. In Proceedings of the 2018 International Energy Conversion Engineering Conference, Cincinnati, OH, USA, 9–11 July 2018; American Institute of Aeronautics and Astronautics: Reston, VA, USA, 2018; p. 34. [CrossRef]

8. van Heerden, A.; Judt, D.M.; Jafari, S.; Lawson, C.P.; Nikolaidis, T.; Bosak, D. Aircraft thermal management: Practices, technology, system architectures, future challenges, and opportunities. *Prog. Aerosp. Sci.* **2022**, *128*, 100767. [CrossRef]
9. Kellermann, H.; Habermann, A.L.; Hornung, M. Assessment of Aircraft Surface Heat Exchanger Potential. *Aerospace* **2020**, *7*, 1. [CrossRef]
10. Kellermann, H.; Habermann, A.; Vratny, P.; Hornung, M. Assessment of fuel as alternative heat sink for future aircraft. *Appl. Therm. Eng.* **2020**, *170*, 114985. [CrossRef]
11. Belov, I.A.; Litvinov, V.M.; Kazakov, A.V.; Kogan, M.N.; Kuparev, V.A. Laminar boundary layer stability and delayed transition on a nonisothermal surface. *Fluid Dyn.* **1989**, *24*, 205–210. [CrossRef]
12. Dovgal, A.V.; Levchenko, V.Y.; Timopeev, V.A. Boundary Layer Control by a Local Heating of the Wall. In *Laminar-Turbulent Transition*; Arnal, D., Michel, R., Eds.; Springer: Berlin/Heidelberg, Germany, 1990; pp. 113–121. [CrossRef]
13. Masad, J.A. Transition in flow over heat–transfer strips. *Phys. Fluids* **1995**, *7*, 2163–2174. [CrossRef]
14. Kametani, Y.; Fukagata, K. Direct numerical simulation of spatially developing turbulent boundary layers with uniform blowing or suction. *J. Fluid Mech.* **2011**, *681*, 154–172. [CrossRef]
15. Lee, J.; Yoon Jung, S.; Jin Sung, H.; Zaki, T.A. Effect of wall heating on turbulent boundary layers with temperature-dependent viscosity. *J. Fluid Mech.* **2013**, *726*, 196–225. [CrossRef]
16. Lin, J.C.; Ash, R.L. Wall temperature control of low-speed body drag. *J. Aircr.* **1986**, *23*, 93–94. [CrossRef]
17. Kramer, B.; Smith, B.; Heid, J.; Noffz, G.; Richwine, D.; Ng, T. Drag reduction experiments using boundary layer heating. In Proceedings of the 37th Aerospace Sciences Meeting and Exhibit, Reno, NV, USA, 11–14 January 1999; American Institute of Aeronautics and Astronautics: Reston, VA, USA, 1999. [CrossRef]
18. Frick, C.W.; McCullough, G.B. *Tests of a Heated Low-Drag Airfoil*; Advance Confidential Report No. 244; National Advisory Committee for Aeronautics: Moffet Field, CA, USA, 1942.
19. Wang, X.; Naterer, G.F.; Bibeau, E. Convective Heat Transfer from a NACA Airfoil at Varying Angles of Attack. *J. Thermophys. Heat Transf.* **2008**, *22*, 457–463. [CrossRef]
20. Norton, D.J.; Macha, J.M.; Young, J.C. Surface Temperature Effect on Subsonic Stall. *J. Spacecr. Rocket.* **1973**, *10*, 581–587. [CrossRef]
21. Longo, J.; Radespiel, R. Numerical simulation of heat transfer effects on two dimensional steady subsonic flows. In Proceedings of the Fluid Dynamics Conference, Bangalore, India, 11–15 July 1994; American Institute of Aeronautics and Astronautics: Reston, VA, USA, 1995. [CrossRef]
22. Lee, J.D. *The Influence of Heat Transfer on the Drag of Airfoils*; Defense Technical Information Center: Fort Belvoir, VA, USA, 1981.
23. Kallath, H.; Kholi, F.K.; Ha, M.Y.; Min, J.K.; Chetwynd-Chatwin, J. Computational study on the aerodynamics of a surface-heated wing for thermal management. *AIAA J.* **2020**, *58*, 4339–4356. [CrossRef]
24. Elsaadawy, E.A.; Britcher, C.P. Effect of Propeller Slipstream on Heat-Exchanger Installations at Low Reynolds Number. *J. Aircr.* **2003**, *40*, 751–758. [CrossRef]
25. Bauhaus Luftfahrt e.V. *Yearbook 2020*; Technical Report; Bauhaus Luftfahrt e.V.: Taufkirchen, Germany, 2020.
26. Economon, T.D.; Palacios, F.; Copeland, S.R.; Lukaczyk, T.W.; Alonso, J.J. SU2: An Open-Source Suite for Multiphysics Simulation and Design. *AIAA J.* **2015**, *54*, 828–846. [CrossRef]
27. Weller, H.G.; Tabor, G.; Jasak, H.; Fureby, C. A tensorial approach to computational continuum mechanics using object-oriented techniques. *Comput. Phys.* **1998**, *12*, 620. [CrossRef]
28. Novelli, P. IMOTHEP: Towards hybrid propulsion for commercial aviation. In Proceedings of the 11th EASN International Conference, Barcelona, Spain, 16 September 2021.
29. Vratny, P.C.; Kaiser, S.; Seitz, A.; Donnerhack, S. Performance investigation of cycle-integrated parallel hybrid turboshafts. *J. Eng. Gas Turbines Power* **2017**, *139*, 031201. [CrossRef]
30. Seitz, A.; Nickl, M.; Stroh, A.; Vratny, P.C. Conceptual study of a mechanically integrated parallel hybrid electric turbofan. *Proc. Inst. Mech. Eng. Part J. Aerosp. Eng.* **2018**, *232*, 2688–2712. [CrossRef]
31. Habermann, A.L.; Kolb, M.G.; Maas, P.; Kellermann, H.; Rischmüller, C.; Peter, F.; Seitz, A. Study of a Regional Turboprop Aircraft with Electrically-Assisted Turboshaft. *Aerospace* 2023, *unpublished*.
32. Seitz, A.; Peter, F. Aircraft Concept for IMOTHEP Conservative Regional Platform Bauhaus Luftfahrt Presentation delivered to ONERA: E-Mail, 21.03.2019.
33. Lednicer, D. The Incomplete Guide to Airfoil Usage. Available online: https://m-selig.ae.illinois.edu/ads/aircraft.html (accessed on 16 March 2023).
34. Drela, M. MSES Overview. Available online: https://web.mit.edu/drela/Public/web/mses/ (accessed on 16 March 2023).
35. Steiner, H.J. *Preliminary Design Tool for Propeller-Wing Aerodynamics, Version v0.44: Part I: Implementation and Reference Manual*; Technical Report; Bauhaus Luftfahrt e.V.: Taufkirchen, Germany; Technical University Munich: Munich, Germany, 2011.
36. Wilkinson, S.P. Interactive Wall Turbulence Control. In *Viscous Drag Reduction in Boundary Layers*; Bushnell, D.M., Hefner, J.N., Eds.; American Institute of Aeronautics and Astronautics: Reston, VA, USA, 1990; Volume 1, pp. 479–509. [CrossRef]
37. Seibert, O. *Heat Transfer of Airfoils and Plates*; Technical Report No. 1044; NASA: Washington, DC, USA, 1943.
38. Baehr, H.D.; Stephan, K. *Heat and Mass Transfer*; Springer: Berlin/Heidelberg, Germany, 2011.
39. Schlichting, H.; Gersten, K. *Boundary-Layer Theory*; Springer: Berlin/Heidelberg, Germany, 2017.
40. Mabey, D.G. Effects of heat transfer on aerodynamics and possible implications for wind tunnel tests. *Prog. Aerosp. Sci.* **1990**, *27*, 267–303. [CrossRef]

41. Reynolds, W.C.; Kays, W.M.; Kline, S.J. A Summary of Experiments on Turbulent Heat Transfer From a Nonisothermal Flat Plate. *J. Heat Transf.* **1960**, *82*, 341–348. [CrossRef]
42. Van Driest, E.R. Calculation of the Stability of the Laminar Boundary Layer in a Compressible Fluid on a Flat Plate with Heat Transfer. *J. Aeronaut. Sci.* **1952**, *19*, 801–812. [CrossRef]
43. Anderson, J.D. *Introduction to Flight*, 8th ed.; McGraw-Hill Series in Aeronautical and Aerospace Engineering; McGraw-Hill Education: New York, NY, USA, 2016.
44. Lin, P.; Liu, X.; Xiong, N.; Wang, X.; Shang, M.; Liu, G.; Tao, Y. Numerical study on the influence of wall temperature gradient on aerodynamic characteristics of low aspect ratio flying wing configuration. *Sci. Rep.* **2021**, *11*, 16295. [CrossRef] [PubMed]
45. Li, B.; Sun, Q.; Xiao, D.; Zhang, W. Numerical Investigation of the Aerofoil Aerodynamics with Surface Heating for Anti-Icing. *Aerospace* **2022**, *9*, 338. [CrossRef]
46. *DIN ISO 2533*; Standard Atmosphere. International Organization for Standardization: Geneva, Switzerland, 1975.
47. White, F.M. *Viscous Fluid Flow*, 3rd ed.; McGraw-Hill Series in Mechanical Engineering; McGraw-Hill Higher Education: New York, NY, USA, 2006.
48. Geuzaine, C.; Remacle, J.F. Gmsh: A 3-D finite element mesh generator with built-in pre- and post-processing facilities. *Int. J. Numer. Methods Eng.* **2009**, *79*, 1309–1331. [CrossRef]
49. Palacios, F.; Alonso, J.; Duraisamy, K.; Colonno, M.; Hicken, J.; Aranake, A.; Campos, A.; Copeland, S.; Economon, T.; Lonkar, A.; et al. Stanford University Unstructured (SU2): An open-source integrated computational environment for multi-physics simulation and design. In Proceedings of the 51st AIAA Aerospace Sciences Meeting Including the New Horizons Forum and Aerospace Exposition, Texas, TX, USA, 7–10 January 2013. [CrossRef]
50. Slater, J.W. Examining Spatial (Grid) Convergence. Available online: https://www.grc.nasa.gov/www/wind/valid/tutorial/spatconv.html (accessed on 16 March 2023).
51. Saetta, E.; Russo, L.; Tognaccini, R. Implementation and validation of a new actuator disk model in SU2. In Proceedings of the SU2 Conference, Virtual, 10–12 June 2020.
52. OpenCFD Ltd. *OpenFOAM Extended Code Guide Version v2012*; OpenCFD Ltd.: Bracknell, UK, 2021.
53. OpenCFD Ltd. *OpenFOAM User Guide Version v2012*; OpenCFD Ltd.: Bracknell, UK, 2020.
54. Poling, B.E.; Prausnitz, J.M.; O'Connell, J.P.; Reid, R.C. *The Properties of Gases and Liquids*, 5th ed.; McGraw-Hill: New York, NY, USA, 2001.
55. NASA. *2D Zero Pressure Gradient Flat Plate Validation Case*; NASA: Washington, DC, USA, 2020.
56. Poinsatte, P.; Van Fossem, G.; Dewitt, K. Convective heat transfer measurements from a NACA 0012 airfoil in flight and in the NASA Lewis Icing Research Tunnel. In Proceedings of the 28th Aerospace Sciences Meeting, Reno, NV, USA, 8–11 January 1990; p. 199.
57. Rumsey, C. 2D NACA 0012 Airfoil Validation Case. Available online: https://turbmodels.larc.nasa.gov/naca0012_val.html (accessed on 16 March 2023).
58. Samuelsson, I. Low speed propeller slipstream aerodynamic effects. In *AGARD, A Selection of Experimental Test Cases for the Validation of CFD Codes*; Advisory Group for Aerospace Research and Development (AGARD): Neuilly-Sur-Seine, France, 1994; Volume 2.
59. Gregory, N.; O'Reilly, C. *Low-Speed Aerodynamic Characteristics of NACA0012 Aerofoil Section, Including the Effects of Upper-Surface Roughness Simulating Hoar Frost*; Technical Report 3762; Aeronautical Research Council: London, UK, 1970.
60. Samuelsson, I. Low speed wind tunnel investigation of propeller slipstream aerodynamic effects on different nacelle/wing combinations. In Proceedings of the 16th ICAS Congress, Jerusalem, Israel, 28 August–2 September 1988; pp. 1749–1765.
61. Samuelsson, I. Experimental Investigation of Low Speed Model Propeller Slipstream Aerodynamic Characteristics including Flow Field Surveys and Nacelle/Wing Static Pressure Measurements. In Proceedings of the 17th ICAS Congress, Stockholm, Sweden, 9–14 September 1990; pp. 71–84.
62. Schultz-Grunow, F. *New Frictional Resistance Law for Smooth Plates*; Technical Report 986; National Advisory Commitee for Aeronautics: Hampton, VA, USA, 1941.
63. Churchill, S.; Bernstein, M. A correlating equation for forced convection from gases and liquids to a circular cylinder in crossflow. *J. Heat Transf.* **1977**, *99*, 300–306. [CrossRef]
64. Hilpert, R. Wärmeabgabe von geheizten Drähten und Rohren im Luftstrom. In *Forschung auf dem Gebiet des Ingenieurwesens;* Springer: Berlin/Heidelberg, Germany, 1933.
65. Wang, X.; Bibeau, E.; Naterer, G. Experimental correlation of forced convection heat transfer from a NACA airfoil. *Exp. Therm. Fluid Sci.* **2007**, *31*, 1073–1082. [CrossRef]
66. Kumar, A.V.M.; Rajendrakumar, N.; Gogineni, P.C.; Gopan, N.; Thangeswaran, R.S.K. Effect of temperature on the aerodynamics of airfoil in low Reynolds number flow. In Proceedings of the International Conference on Applied Mechanics and Optimisation, Thiruvananthapuram, India, 13–15 June 2019; AIP Publishing: College Park, MD, USA, 2019. [CrossRef]
67. Kellermann, H.; Habermann, A.L.; Seitz, A. Thermal Management System Design for a Regional Hybrid Electric Aircraft. *Aerosp. Eur. Conf.* 2023, *unpublished*.
68. Chakraborty, I. Subsystem Architecture Sizing and Analysis for Aircraft Conceptual Sesign. Ph.D. Thesis, Georgia Institute of Technology, Atlanta, GA, USA, 2015.
69. Menter, F.R. Two-equation eddy-viscosity turbulence models for engineering applications. *AIAA J.* **1994**, *32*, 1598–1605. [CrossRef]
70. Wilcox, D.C. *Turbulence Modeling for CFD*, 3rd ed.; DCW Industries: La Cañada, CA, USA, 2006.

71. McLean, D. *Understanding Aerodynamics: Arguing from the Real Physics*; Wiley: Hoboken, NJ, USA, 2013.
72. Menter, F.R.; Sechner, R.; Matyushenko, A. Best Practice: RANS Turbulence Modeling in Ansys CFD: Version 1.0. 2021. Available online: https://www.google.com/url?sa=t&rct=j&q=&esrc=s&source=web&cd=&ved=2ahUKEwiIltqCp8X-AhX3cPEDHW36DGYQFnoECCQQAQ&url=https%3A%2F%2Fwww.ansys.com%2Fcontent%2Fdam%2Famp%2F2022%2Ffebruary%2Fasset-creation%2Fbest-practices-campaign%2FBest%2520Practice-Rans%2520turbulence%2520modeling%2520in%2520Ansys%2520CFD.pdf&usg=AOvVaw1QBesb85eewbczguddwvJs (accessed on 15 March 2023).

Disclaimer/Publisher's Note: The statements, opinions and data contained in all publications are solely those of the individual author(s) and contributor(s) and not of MDPI and/or the editor(s). MDPI and/or the editor(s) disclaim responsibility for any injury to people or property resulting from any ideas, methods, instructions or products referred to in the content.